2017

Reduced Order Models for Beam-Wave Interaction in High Power Microwave Sources

Lokendra Singh Thakur
Louisiana State University and Agricultural and Mechanical College

REDUCED ORDER MODELS FOR BEAM-WAVE INTERACTION IN HIGH POWER MICROWAVE SOURCES.

A Dissertation

Submitted to the Graduate Faculty of the
Louisiana State University and
Agricultural and Mechanical College
in partial fulfillment of the
requirements for the degree of
Doctor of Philosophy

in

The Department of Mathematics

by
Lokendra Singh Thakur
M.S. in Math., Louisiana State University, May 2012
August 2017

Acknowledgments

Mother gives life and teacher shapes the life through his or her teachings. Which makes the life to live with respect in the society. So, no matter what I do in my life the credit will always go to my mother because she not only gave me birth but also taught me how to live life with character. Life gets nurtured well only when family environment is caring, lovable and financially stable. Thus, I will share my success with my brothers, sister, and each member of my family. When I look at a pound of recognizing faces without their contributions and help I would not be standing where I am as a mathematician. The first face which blossoms as a lotus and shine even on a cloudy day is my advisor Professor Robert Lipton. The credit for molding my chemistry and life sciences point of view and thinking into a logical and rigorous mathematical one goes to him. Second is of Professor Leonard Richardson for believing in me and giving me an opportunity to prove myself by offering an admission into the masters program otherwise my desire for learning mathematics would not have been fulfilled. Thirdly Professor Milen Yakimov for giving his time for answering my questions in my first semester. I am also thankful to my colleague Dr. Anthony Polizzi. Finally, I acknowledge my mathematics department's professors, administrative and technical staff.

Table of Contents

Abstract

We apply an asymptotic analysis to show that corrugated waveguides can be represented as cylindrical waveguides with smooth metamaterial coatings when the corrugtions are subwavelength. Here the metamaterial delivers an effective anisotropic surface impedance, effective dielectric constant, and imparts novel dispersive effects on signals traveling inside the waveguide. These properties arise from the subwavelength resonances of the metamaterial. For sufficiently deep corrugations, the waveguide exhibits backward wave propagation, which can be understood in the present context as a multi-scale phenomenon resulting from local resonances inside the subwavelength geometry. Our approach is well suited to numerical computation and we provide a systematic investigation of the effect of corrugation geometry on wave dispersion, group velocity, power flow, and gain factor per period.

Chapter 1
History of the Problem

1.1 introduction

Vacuum electronic devices (VED) because of its applications in radar, space and terrestrial communication, fusion, industrial processing, medicine, and microwave ovens secured place at the heart of modern technologies. This is the reason that VED is an active domain of research both in the corporate and academic worlds.

1.2 vacuum electronic devices history

Most microwave sources were invented prior to World War II and it germinated from the seed sowed in the year 1897, when J. J. Thomson identified the cathode ray in a vacuum tube. In 1904, J. A. Fleming discovered the diode, the first vacuum tube, and in 1906 Lee de Forest built the triode by adding a third electrode to the diode. These discoveries flourished the 1920's broadcasting and the radio-links [21]. The magnetron and reflex klystron were invented in the 1930's and were the subject of intense development efforts during World War II for use in radar. Rudolf Kompfner, in early November 1943, invented the new device, initially known as a "Helical coaxial-line," later popularly labelled as a "traveling wave tube" (TWT). He had obtained amplification from an experimental tube for the first time [17]. In 1944, John R. Pierce learned about this TWT during his visit to the Clarendon Laboratory at Oxford University in England. In December 1947, Pierce's colleagues, Walter Brattain and John Bardeen, produced amplification using a semiconductor triode. Pierce is credited with proposing the name "transistor" for the new amplifier prior to the public announcement of the invention in May 1948. In March 1959, Pierce and Kompfner published an IRE paper titled "Transoceanic Communications by means of Satellites." On 10 July 1962 the launch of the active

repeater satellite known as "Tel star" was designed as a communication satellite by Bell engineers. This project under Pierce's leadership marked the beginning of satellite communication [17]. In 1964 the gyrotron was invented in Russia. These were experimentalist-led microwave sources. Therefore this period of developments in VED is known as an era of experimentalist-led microwave sources. Followed by experimentalist led high power microwave sources, which experienced a paradigm shift and finally led into the current era of metamaterial high power microwave sources as discussed in history of the problem section. Moreover, the urge to know the evolution, current era along with the possible attainable efficiency and future of the microwave sources just at a glance has led to the creation of VED clock in Figure.1.1. The history of vacuum electronic devices starts clockwise. Each sector represents an era and a dash line in a sector mean an inception of a new era.

1.3 formulation of the problem

The second quadrant in Figure.1.1 starts from the late 1960s until the early 1990s, which we call the experimentalist led high power microwave (HPM) era. The researchers in this era were striving to achieve ever-greater output power levels by designing and developing HPM sources. Early-to-mid 1990s experienced a paradigm shift, during this shift prototyping evolved to such an extent that computer simulations of devices overtook the experimentalists in exploration of new source concepts [22]. The prototyping offers economies of scale and also motivation to explore new source concepts. Because a prospective source concepts are thoroughly investigated through computer simulations and prototyping till it provides a robust and worthy design and then the hardware is built for that design. A new era in HPM source design shown in Figure.1.1, set the inception of metamaterial HPM era. This era is about exploiting metamaterials and photonics band gab structures for dispersion engineering. Metamaterials and electromagnetic band gap structures are of

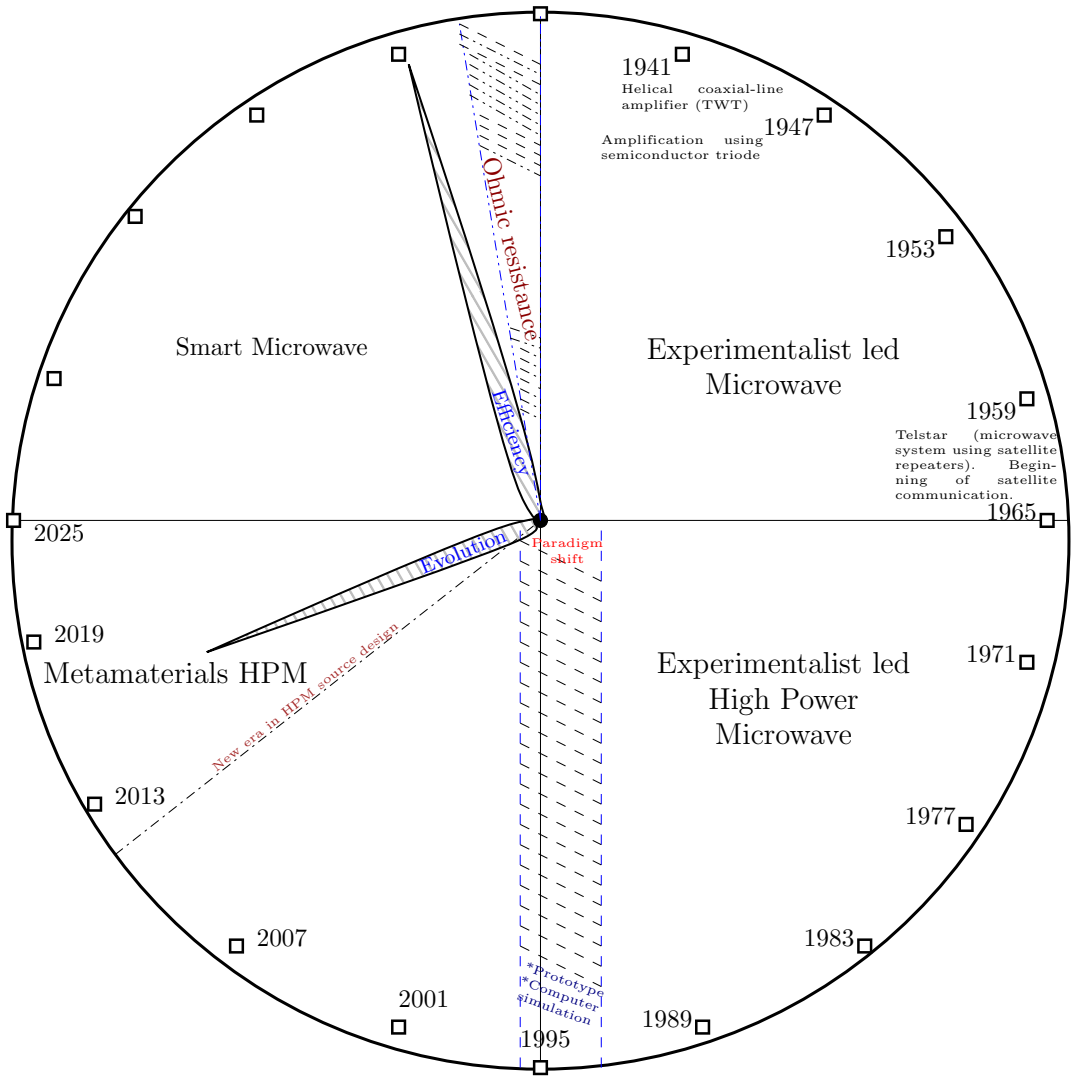

FIGURE 1.1. VED clock

interest for vacuum electron sources for high power microwave structures. Such structures provide for wave velocity control critical to realizing high power traveling wave tubes and dielectric Cerenkov maser amplifiers/oscillators [22]. However, as noted by Shiffler et al. in [16], dielectrics become vulnerable to charging, resulting in device failure. In spite of these limitations, they note that it is important to "explore and exploit the unique physics of relativistic electron beam driven metamaterial devices. The key advance manifested here consists of the concept of finding a metallic sub-wavelength structure, or metamaterial, that mimics the

response of a dielectric for generating slow electromagnetic waves." In this article the authors demonstrated for the first time the use of all-metal metameterials to generate Cerenkov-like masers interactions. But the same article did not have a systematic theory and methodology. These concerns lead to the formulation of the problem for the thesis.

Chapter 2
Physics Background

2.1 introduction

Radio technology (RT) in its nascent stages of development utilized only the low end of the frequency spectrum. As the number of users and applications increased over the period of time, confusion and conflict ocurred in the areas of transmission and reception, because of overpopulated lower range of the radio frequency (RF) spectrum. An international conventions had formed to fix this problem by allocating the usable frequency spectrum among the national and international research and other services. RT evolution led it to move up in the frequency spectrum. As a result by the start of World War II, the band width requirements of the sophisticated communication equipment were in the microwave region. Increase in frequency means decrease in wavelength, which created a problem because the equipment component's geometry is comparable to the wavelengths used. This problem motivated scientists and their research led to the solution, known as Transmission Line Theory. In microwave range Transmission Line Theory, Distributed Line Analysis and Electromagnetic Field Theory are used to analyze circuits operation. Modern technology is based on microwaves for example at corporate level television, national and local securities, communication networks and at consumer level microwave ovens, etc.,. The field is progressing and growing very fast.

2.2 challenges

In the high power regime the first challenge is traditional dielectric materials are not practical because after few operational cycles, the ions accumulate in the dielectric. As a result, the dielectric material incurs stresses due to high fields and is either damaged or fails. In [16], the use of subwavelength, periodic, perfect conductor-

interaction structure is proposed, which effectively acts as a dielectric material with dielectric constant >1. The second challenge is the causes for reflections as mentioned in [5].

2.3 comparison of hpm sources

A periodic all metal interaction structure is considered. In an amplifier, Bloch wave solutions of Maxwell's equations are driven by an electron beam confined to a radius $0 < r < R_b$. The hydrodynamic approximation is used and the beam current is J_z directed along the z direction and is related to the z directed electric field E_z of the propagating wave by the constitutive law $J_z = \alpha E_z$. The parameter α depends on the wave number k of a Bloch wave and is given by $\alpha = \frac{\omega_p^2}{\gamma^3 v_0^2 (\frac{\omega}{v_0} - k)^2}$. Where γ is the relativistic correction and ω_p is the plasma frequency [18], [19]. We denote the wave number in the absence of the beam by k_0 and for this case $\alpha = 0$ (cold structure). We then consider nonzero α (hot structure). Using this set-up we formally expand solutions in powers of δk and α. On equating powers the leading order theory provides a dispersion relation between frequency and δk. The dispersion relation is given by a third order polynomial. The polynomial is similar to that given in the Pierce theory of microwave amplifiers and amplification occurs when δk is complex and has positive imaginary part [5]. The coefficients of the polynomial are calculated numerically and depend on the geometry of the interaction structure. In an oscillator, expand the standing wave solutions in powers of $\delta\omega$ and α by imposing perfect boundary conditions at $z = 0$ and $z = d$ instead of floquet periodic conditions and follow the procedure as mentioned for amplifiers to get rise time.

2.4 metamaterial geometry

High power microwave source is made from a dielectrically loaded wave guide. The macroscopic view in Figure. 2.1 is the metamaterial view visible to the naked eye

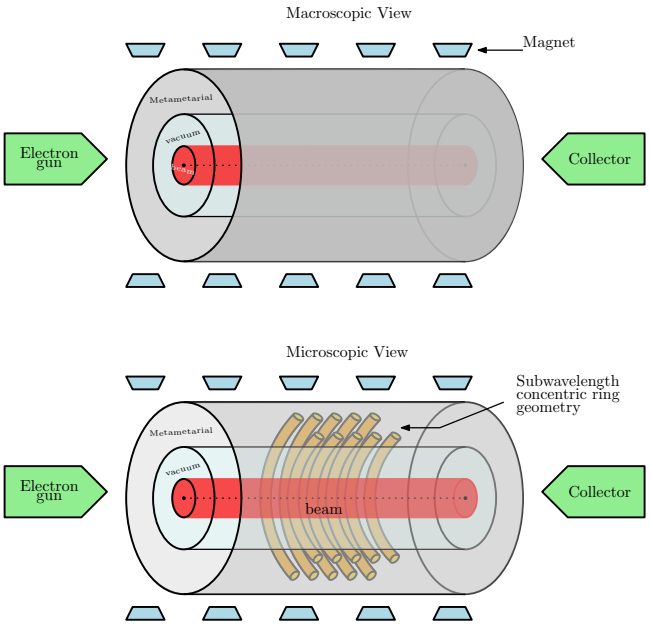

FIGURE 2.1. Macro and microscopic view of the geometry

and the microscopic one in Figure. 2.1 demonstrates the involved subwavelength periodic concentric ring microstructures in the construction of the metamaterial. Design of the subwavelength microstructures will tune its dielectric constant, which is otherwise not possible considering only naturally occurring materials.

2.5 mechanism

An electron beam from the gun in Figure. 2.1 and an electromagnetic (EM) wave from an input is injected. The beam is kept focused at the center by the magnetic fields and an EM wave propagates through the metamaterial region in Figure. 2.1. Amplification will occur, provided the metamaterial slows the phase velocity of the EM wave below the velocity of light in a vacuum. Hence, we require a dielectric constant >1. When the phase velocity of the EM wave matches the velocity of electrons in the beam, energy transfers from electrons to the EM wave. Thus, the EM wave gets maximum gain. The amplified pulse is collected by the collector.

2.6 engineering dispersion curves

An interaction of an electromagnetic wave with a material results in a phenomenon called dispersion. The curve which shows this phenomenon as a relationship between a wave number and frequency is known as a dispersion curve. The metamaterial paradigm provides tools such as, all-metal subwavelength microstructures, design geometry of the microstructure, and adjust subwavelength spacing between the microstructures. Which helps in engineering dispersion curves.

Chapter 3
Mathematics Background

3.1 homogenization theory and metamaterials

Starting from the microscopic, rapidly varying coefficients of a problem, we seek a slowly varying macroscopic, or "homogenized" or "effective", systems of equations in which the fine-scale structure is averaged out in an appropriate way. Indeed, in many fields of science and technology one has to solve boundary value problems in periodic media with period say d. Quite often the size of the period is small compared to the size of a sample of the medium, and, denoting by η their ratio, an asymptotic analysis, as η goes to zero, is called for. This process of making an asymptotic analysis and seeking an averaged formulation A^h is called homogenization. Homogenization was first developed for periodic structures. In the present section we focus on the homogenization of periodic structures. The method of two-scale asymptotic expansions is presented, and its mathematical justification will be briefly discussed. However, the homogenization is not restricted to the periodic case and can be applied to any kind of disordered media. The notion of G- or H-convergence allows one to consider any possible geometrical situation without any specific assumptions like periodicity or randomness. Fundamental and physically important phenomena are modeled by second-order linear elliptic partial differential equations (PDEs). So, we will consider the homogenization of it but similar ideas apply to many other types of linear and nonlinear PDEs.

periodic homogenization

Consider a $\Gamma \subseteq R^2$ homogeneous anisotropic conductor with conductivity tensor A. The domain Γ is segmented into Q of size unit length and Q is periodic in x_1 and x_2 axes. Focusing on a single cell Q, represent the involved dielectrics as host

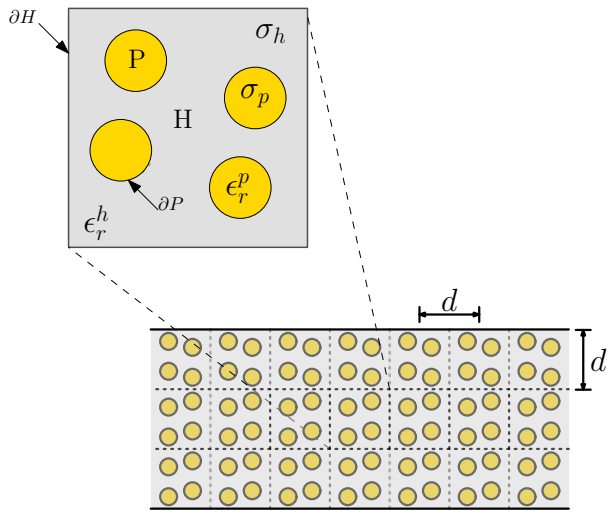

FIGURE 3.1. Anisotropic composite medium

H and inclusion P or inclusions $\sum_{i=1}^{n} P_i$. For the present discussion, we consider $Q = H \cup P$ with ϵ_r^p, σ_p and ϵ_r^h, σ_h as their respective dielectrics and conductivities.

ansatz

We assume a two phase periodic conductor with conductivity: $a(\vec{x}) = \sigma_p \chi_p(\vec{x}) + \sigma_h \chi_h(\vec{x})$, such that $\chi_p(\vec{x}) = 1 - \chi_h(\vec{x})$, where

$$\chi_p = \begin{cases} 1 & \text{in } P \\ 0 & \text{in } H \end{cases} \qquad and \qquad \chi_h = \begin{cases} 1 & \text{in } H \\ 0 & \text{in } P. \end{cases} \tag{3.1}$$

Next we introduce the parameter 'd' to denote the scale of the periodic structure. Let $a^d(\vec{x}) = a(\frac{\vec{x}}{d}) = \sigma_p \chi_p(\frac{\vec{x}}{d}) + \sigma_h \chi_h(\frac{\vec{x}}{d})$ then Temperature $T^d(x_1, x_2)$ has (1) Linear component: $d \cdot \vec{x}$. and (2)Q-periodic one with $|Q| = 1$, oscillates with the geometry. Thus, $T^d(x_1,x_2) = T^d(\vec{x}) = d \cdot \vec{x} + v(\vec{x})$; $v = v^d$ depends upon the linear component.

textbfProcedure

We consider the Dirichlet problem with T^d=$T^d(x_1,\, x_2)$ as the solution of

$$\begin{cases} -\nabla\cdot(a(\frac{\vec{x}}{d})\nabla T^d) = f, \text{in domain } \Gamma \\ n\cdot(\sigma_p\nabla T^d)_{|_{\partial p^-}} = n\cdot(\sigma_h\nabla T^d)_{|_{\partial p^+}}, \text{on } \partial P \\ T^d = 0, \text{on } \partial\Gamma. \end{cases} \tag{3.2}$$

The Fundamental Theorem of Periodic Homogenization says that the solution T^d converges to a limit T^h as $d \to 0$, which solves the homogenized Dirichlet problem,

$$\begin{cases} -\nabla\cdot(A^h\nabla T^h) = f, \text{in domain } \Gamma \\ T^h = 0, \text{on } \partial\Gamma. \end{cases} \tag{3.3}$$

where A^h is a constant 2×2 matrix representing effective property of the material. We define A^h by $A^h_{ij} = \int_Q a(y)(\nabla v^i + e^i)\cdot(\nabla v^j + e^j)dy_1dy_2.$, where $v^i(y_1, y_2)$ solves the cell problem.

$$\begin{cases} -\nabla\cdot(a(y)\nabla v^i) = 0, \text{in domain } Q \\ n\cdot(\sigma_p\nabla(v^i+e^i))_{|_{\partial p^-}} = n\cdot(\sigma_h\nabla(v^i+e^i))_{|_{\partial p^+}}, \text{on } \partial P \\ v^i = 0, \text{on } \partial Q. \end{cases} \tag{3.4}$$

derivation of A^h_{ij} using two scale asymptotic expansions

We assume two scales a fast scale $(y_1, y_2) = (\frac{x_1}{d}, \frac{x_2}{d})$ and a slow scale $(x_1,\, x_2)$ such that $T^d = T(x_1, x_2, y_1, y_2)$ then the operation of $x_1,\, x_2$ differentiation becomes $\partial_{x_i}T = \partial_{x_i}T + \frac{1}{d}\partial_{y_i}T$, here ∂_{y_i} $i = 1, 2$ represents differentiation with respect to the fast variables. Thus $\nabla T = \nabla_x T + \frac{1}{d}\nabla_y T$ and we rewrite the unhomogenized dirichlet problem as a two-scale Dirichlet problem,

$$\begin{cases} -(\nabla_x + \frac{1}{d}\nabla_y)\cdot(a(\frac{\vec{x}}{d})(\nabla_x + \frac{1}{d}\nabla_y)T) = f, \text{in domain } \Gamma \\ n\cdot(\sigma_p(\nabla_x + \frac{1}{d}\nabla_y)T)_{|_{\partial p^-}} = n\cdot(\sigma_h(\nabla_x + \frac{1}{d}\nabla_y)T)_{|_{\partial p^+}}, \text{on } \partial P \\ T = 0, \text{on } \partial\Gamma. \end{cases} \tag{3.5}$$

Moreover we represent T^d in terms of the asymptotic series, $T^d = T^0(x_1, x_2, y_1, y_2) + dT^1(x_1, x_2, y_1, y_2) + d^2T^2(x_1, x_2, y_1, y_2) + \ldots$, now we substitute the expansion in the two-scale Dirichlet problem 3.5, and by collecting like powers of d give the various order differential equations:

$$\begin{cases} \text{Order } d^{-2} : (a)0 = \nabla_y \cdot (a(y)\nabla_y T^0). \\ \text{Order } d^{-1} : (b)0 = [n \cdot (a(y)\nabla_y T^0)]_{\sigma_h}^{\sigma_p}, \\ (c)0 = \nabla_x \cdot (a(y)\nabla_y T^0) + \nabla_y \cdot (a(y)\nabla_x T^0) + \\ +\nabla_y \cdot (a(y)\nabla_y T^1). \\ \text{Order } d^0 : (d)0 = [n \cdot a(y)(\nabla_x T^0 + \nabla_y T^1)]_{\sigma_h}^{\sigma_p}, \\ (e)0 = -\nabla_x \cdot (a(y)\nabla_x T^0) - \nabla_x \cdot (a(y)\nabla_y T^1) - \\ -\nabla_y \cdot (a(y)\nabla_x T^1) - \nabla_y \cdot (a(y)\nabla_y T^2). \\ \text{Order } d^1 : (f)0 = [n \cdot a(y)(\nabla_x T^1 + \nabla_y T^2)]_{\sigma_h}^{\sigma_p}. \end{cases} \tag{3.6}$$

From this system of equations, we can derive the zero order Dirichlet problem

$$\begin{cases} \nabla_y \cdot (a(y)\nabla_y T^0) = 0, \text{in domain } \Gamma \\ n \cdot (\sigma_p \nabla_y T^0)_{|_{\partial p^-}} = n \cdot (\sigma_h \nabla_y T^0)_{|_{\partial p^+}}, \text{on } \partial P \\ T^0 = 0, \text{on } \partial\Gamma. \end{cases} \tag{3.7}$$

T^0 solves the problem 3.7, and since $T^0(x, y) = T^0(x)$, we have

$$\begin{cases} \text{(c) in equation 3.6 becomes,} \\ \nabla_y \cdot (a(y)\nabla_x T^0) + \nabla_y T^1) = 0. \\ \text{(d) in equation 3.6 becomes,} \\ [n \cdot a(y)(\nabla_x T^0 + \nabla_y T^1)]_{\sigma_h}^{\sigma_p} = 0. \end{cases} \tag{3.8}$$

Here $T^1 = T^1(x,y)$, $x \in \Gamma$ and $y \in Q$(periodic cell). For a fixed x we have

$$\begin{cases} \nabla_y \cdot (a(y)\nabla_x T^0) + \nabla_y T^1) = 0, \\ [n \cdot a(y)(\nabla_x T^0 + \nabla_y T^1)]_{\sigma_h}^{\sigma_p} = 0. \end{cases} \tag{3.9}$$

and for each x, $T^1(x,y)$ is y-periodic in Q. So, $\nabla_x T^0(x) = e^1 \partial_{x_1} T^0(x) + e^2 \partial_{x_2} T^0(x)$. From linearity, $T^1(x,y) = v_y^1 \partial_{x_1} T^0(x) + v_y^2 \partial_{x_2} T^0(x)$ and $\nabla_y T^1(x,y) = \nabla_y v_y^1 \partial_{x_1} T^0(x) + \nabla_y v_y^2 \partial_{x_2} T^0(x)$. Thus, $T^1(x,y) = v_y^1 \partial_{x_1} T^0(x) + v_y^2 \partial_{x_2} T^0(x)$. By integrating both sides of (e) in equation 3.6 with respect to y over the unit cell, we get

$$\begin{cases} \int_Q f(x)dy = \int_Q [-\nabla_x \cdot (a(y)(\nabla_x T^0 + \nabla_y T^1) - \nabla_y \cdot (a(y)(\nabla_x T^1 + \nabla_y T^2)))]dy, \end{cases} \tag{3.10}$$

Applying integration by parts we obtain

$$\begin{cases} f(x) = -\nabla_x \cdot \int_Q (a(y)(\nabla_x T^0 + \nabla_y T^1)dy, \end{cases} \tag{3.11}$$

and from the ansatz on T^1 we have

$$\begin{cases} f(x) = -\nabla_x \cdot \sum_{i=1}^{2} \int_Q (a(y)(e^i + \nabla_y v^i(y))dy \partial_{x_i} T^0, \\ \text{or,} \\ f(x) = -\nabla \cdot (A^h \nabla T^0). \end{cases} \tag{3.12}$$

where we define the effective dielectric tensor A^h by

$$A_{ij}^h = \int_Q a(y)(e_j^i + \partial_{y_j} v^i)dy. \tag{3.13}$$

Chapter 4
Novel Metamaterial Surfaces

4.1 overview

Motivated by numerical experiments carried out in [12], we construct cylindrical waveguides in which the outer walls are perfect conductors with periodic corrugations. We begin with the time harmonic Maxwell's equations in the waveguide. Assuming a subwavelength scale of corrugations, we expand the electric and magnetic fields in the waveguide as series in the period of the corrugations. We homogenize the rough surface of the waveguide in $z-$axis when the period d of the corrugation goes to zero. Here the depth h of the corrugations is kept fixed as the period is sent to zero. The fields in the leading order theory now satisfy Maxwell's equations on a smooth circular cylinder with anisotropic impedance boundary conditions. In this way, the subwavelength variations in waveguide geometry are manifested only by an effective surface impedance condition 4.18 imposed on a simpler problem 4.22. This allows us to recover an effective surface impedance that captures the resonance frequencies of local TM modes inside subwavelength chambers between corrugations. These resonances appear as poles in the effective surface admittance 4.24, and creates backward wave propagation for a sufficiently deep corrugations. This approach is well suited to numerical computation, and we provide a systematic investigation of the effect of corrugation geometry on wave dispersion, group velocity, and power flow.

4.2 introduction

We construct cylindrical waveguides in which the outer walls are perfect conductors with periodic corrugations. This type of waveguide is well known in the microwave literature [14]. We show that, if the longitudinal scale of the corrugation geometry

is sufficiently small, the entire waveguide can be effectively modeled as a smooth cylindrical waveguide surrounded by a metamaterial impedance layer that captures the effects of the corrugation geometry.

We begin with Maxwell's equations in the waveguide. Assuming a subwavelength scale of corrugations, we expand the electric and magnetic fields in the waveguide as series in the period of the corrugations. Passing to the limit of vanishing period our analysis replaces Maxwell's equations in the corrugated region of the waveguide with an effective surface impedance condition for the leading order theory of the series expansion. The fields in the leading order theory now satisfy Maxwell's equations on a smooth circular cylinder with anisotropic impedance boundary conditions. In this way, subwavelength variations in waveguide geometry are manifested only in an effective impedance condition imposed on a simpler problem. The homogenized waveguide recovers trends seen in direct numerical simulation [12] and is well suited to the fast numerical computation of dispersion relations, group velocities, power flows, etc., given below in section 4.5.

background, motivation, and main results

Our work is motivated by the study of backward wave propagation in corrugated waveguide structures, specifically, the observation that waveguides with sufficiently deep corrugations support backward waves, see [12]. Early on, this was discovered in a heuristic way and exploited in [9] for infinitely thin corrugations in cylindrical waveguides. This is further investigated in more recent work [11]. These works employ the so-called surface impedance method [9], [10], in which infinitely thin corrugations of a waveguide are replaced with a smooth wall having a non-isotropic but uniform impedance. Here we depart from the earlier work and show that it is possible to recover an effective surface impedance model directly from Maxwell's equations for subwavelength corrugations through asymptotic analysis. We show

an effective impedance is a purely subwavelength phenomenon and naturally arises without having to assume infinitely thin corrugations as in [9] and [11]. It is emphasized that unlike the effective impedance layer treated in [13] we do not assume that the depth of the corrugations is small relative to the radius of the waveguide. This feature is necessary for understanding the effect of corrugation depth on wave dispersion inside the waveguide. Our study unambiguously shows that the presence of negative group velocity hybrid modes is a multiscale phenomenon that is captured directly from Maxwell's equations using asymptotic analysis. It is found that the negative group velocity arises from subwavelength resonances generated inside the chambers associated with the corrugated boundary see 4.1. In this way we see that the corrugated boundary functions as a true metamaterial influencing dispersion at wavelengths longer than the period of the corrugations.

The asymptotic analysis and effective impedance layer developed here recover the simpler surface impedance associated with infinitely thin ribs reported in the microwave literature in the mid 20^{th} century, see Clarricoats *et. al.*, [9]. Our analysis shows that more general corrugations result in different effective surface impedances. For a given subwavelength corrugation profile, our method is applied to compute dispersion relations, group velocities, and power flow within the waveguide. In particular, we use our model to study the effect of the corrugation depth on a waveguide's ability to support backward waves. The results presented in 4.5 strongly affirm the results of the numerical investigation [12] that points to the existence of metamaterial phenomena inside corrugated waveguides. This behavior is also corroborated in the recent work of [11].

approach

In this dissertation section we develop two-scale asymptotic expansions [6], [4]. This method has been applied to problems involving rough interfaces and rough

boundaries in [3], [2], [1]. We employ this approach to homogenize the rough surface of the waveguide when the period d of the corrugation goes to zero. Here the depth of the corrugations is kept fixed as the period is sent to zero. This together with the perfect conducting boundary condition allows us to recover an effective surface impedance that captures the resonance frequencies of local TM modes inside subwavelength chambers between corrugations, see 4.9 and 4.12–4.16. These resonances appear as poles in the effective surface admittance $\mathcal{Y}_{ad}$ and are plotted in Figures 4.7a to 4.9. The local resonances are seen to directly effect the dispersive properties of the waveguide through the leading order dispersion relation given by Propositions 4.1 and 4.2.

The work is organized as follows: The physical model is presented in 4.3. The method of two-scale expansion is described in 4.3. The general formulation of the leading order theory for time harmonic Maxwell's equations is presented in 4.3. In 4.3, we present the effective surface admittance/impedance associated with hybrid modes. The effect of local resonances on the effective admittance and wave dispersion is illustrated numerically in 4.4 and the effect of corrugation depth is explored in 4.5. The two-scale asymptotic derivation of the model is presented in 5.6.

4.3 model description

We assume a cylindrical waveguide of infinite length. The outer metallic shell of the waveguide has periodic corrugations with no azimuthal variation. The radius of the waveguide does not exceed $r_m + h$, and the corrugation depth does not exceed h. Hence, the region of the waveguide with subwavelength periodic variation is contained in the annular domain $\{r \mid r_m \leq r \leq r_m + h\}$; see 4.2. The the (longitudinal) period of the corrugations is small relative to the inner radius r_m and given by d.

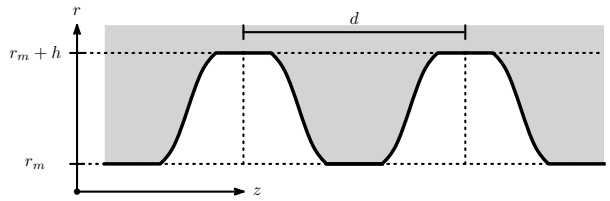

FIGURE 4.1. Truncated sinusoidal corrugations in annular domain $\{r \mid r_m \leq r \leq r_m+h\}$ of cylindrical waveguide

In this study, we employ d-periodic sinusoidal, saw tooth, and rectangular corrugations, see 4.3. The corrugation shape is initially defined on a unit period, and the corrugations are described on rescaling by d. We define the corrugation profile through the shape function $\theta(r)$ defined for $r_m < r < r_m + h$; here $\theta(r) > 0$ and $|\theta(r)'| < \infty$, see Figure 4.4.

Within the waveguide, we assume a vacuum, while the surrounding metallic wall is treated as a perfect conductor. Thus, the electric and magnetic fields in the waveguide satisfy Maxwell's equations inside the corrugated wall, satisfy the conditions of a perfect conductor on the surface of the outer wall, and are zero within the thin conducting shell. Our asymptotic analysis results in a surface impedance model in which periodic corrugations are replaced with an impedance surface surrounding the inner waveguide region $\{r \mid r \leq r_m\}$. For general time-harmonic modes propagating in the waveguide, our effective surface impedance model is described in 4.3 below. In the case of hybrid modes, a mix of transverse electric (TE) and transverse magnetic (TM) fields, we recover a more specific form of the effective surface impedance given in 4.3.

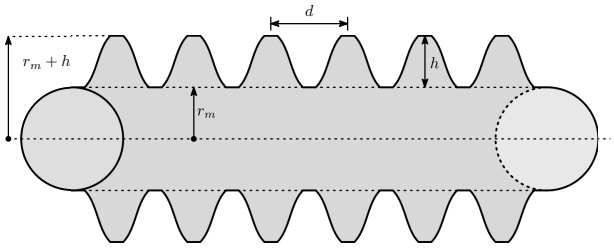

FIGURE 4.2. Corrugated waveguide with d-periodic truncated sinusoidal corrugations

physics of waveguides & maxwell's equations

In this dissertation section, the periodic corrugation is represented by rescaling a unit-periodic geometry (see Figure 4.4) so that the corrugations are unit-periodic in $y = z/d$. The wavelength of a propagating mode is denoted by λ, and we are interested in subwavelength propagation, $d \ll \lambda$. The cylindrical waveguide has corrugated outer walls, and $\theta(r)$ denotes a profile function describing the corrugation shape as a function of r. In this dissertation section, we investigate square corrugation profiles [12] as well as sawtooth, sinusoidal, and infinitely thin rib profiles, see 4.3.

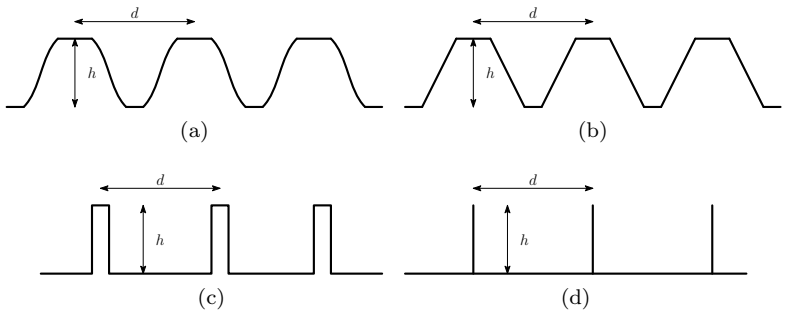

FIGURE 4.3. Corrugation geometries considered: (a) truncated sinusoidal corrugations, (b) truncated sawtooth corrugations, (c) square rib corrugations, (d) infinitely thin corrugations.

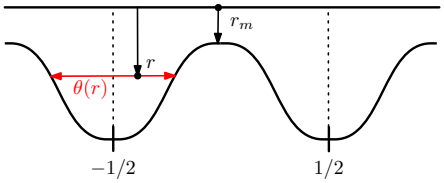

FIGURE 4.4. Unit-periodic geometry with unit-periodic corrugation and profile function $\theta(r)$

We assume that the electric and magnetic fields within the waveguide have the time-harmonic form

$$\mathbf{E} = \mathbf{E}(y, z, r, \varphi)e^{i\omega t}, \qquad \mathbf{B} = \mathbf{B}(y, z, r, \varphi)e^{i\omega t}, \tag{4.1}$$

with $\mathbf{E}$ and $\mathbf{B}$ being unit-periodic in the "fast" y-variable, $y = z/d$. Here, (z, r, φ) denote canonical cylindrical coordinates. $\mathbf{E}$ and $\mathbf{B}$ exhibit both a d-periodic variation in z as well as a slow variation in z.

The waveguide is split into two concentric subdomains, denoted by Ω_W and Ω_I. Here, Ω_W is the cylindrical inner waveguide, $0 < r < r_m$; Ω_I is the cavity region interior to the waveguide domain, $r_m < r < r_m + h$ (see Figure 4.5).

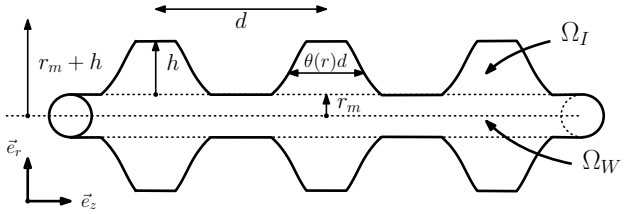

FIGURE 4.5. Domains Ω_I and Ω_W.

The fields inside Ω_W are denoted by $\mathbf{E}^W, \mathbf{B}^W$, and the fields inside Ω_I are denoted by $\mathbf{E}^I, \mathbf{B}^I$. As we adopt $e^{i\omega t}$-time-harmonic behavior, on Ω_W, fields $\mathbf{E}^W, \mathbf{B}^W$ solve the time-harmonic Maxwell's equations

$$\begin{cases} \nabla \times \mathbf{E}^W = -i\omega \mathbf{B}^W, \\ \nabla \times \mathbf{B}^W = i\omega \mu_0 \epsilon_0 \mathbf{E}^W, \\ \nabla \cdot \mathbf{B}^W = 0, \\ \nabla \cdot \mathbf{E}^W = 0, \end{cases} \tag{4.2}$$

and $\mathbf{E}^I, \mathbf{B}^I$ satisfy, on Ω_I,

$$\begin{cases} \nabla \times \mathbf{E}^I = -i\omega \mathbf{B}^I, \\ \nabla \times \mathbf{B}^I = i\omega \mu_0 \epsilon_0 \mathbf{E}^I, \\ \nabla \cdot \mathbf{B}^I = 0, \\ \nabla \cdot \mathbf{E}^I = 0. \end{cases} \tag{4.3}$$

On the outer boundary of the waveguide, denoting the unit outer normal vector field by $\vec{\nu}$, we impose perfect conducting boundary conditions

$$\mathbf{E}^I \times \vec{\nu} = 0, \qquad \mathbf{B}^I \cdot \vec{\nu} = 0. \tag{4.4}$$

The waveguide boundary can have flat parts. Here we recall that the boundary of the waveguide is a metallic shell given by a perfect conductor with zero electric and magnetic fields inside. With this in mind for $r = r_m$, we extend $\mathbf{E}^I$ and $\mathbf{B}^I$ by zero onto the flat parts. We write this observation as

$$\begin{cases} \mathbf{E}^I(y, r_m, z, \varphi) = 0, \text{ for } y_-(r_m) < y < y_+(r_m), \\ \mathbf{B}^I(y, r_m, z, \varphi) = 0, \text{ for } y_-(r_m) < y < y_+(r_m). \end{cases} \tag{4.5}$$

We denote y-averages of a quantity q over the unit period $[-1/2, 1/2]$ by $\langle q \rangle = \int_{-1/2}^{1/2} q(y)dy$, and at $r = r_m$ and we impose the average transmission conditions

$$\begin{cases} \langle \mathbf{E}^W - \mathbf{E}^I \rangle \times \vec{e}_r = 0, \\ \langle \mathbf{B}^W - \mathbf{B}^I \rangle \times \vec{e}_r = \mathbf{J}(r, \varphi, z), \\ \langle \epsilon_0 \mathbf{E}^W - \epsilon_0 \mathbf{E}^I \rangle \cdot \vec{e}_r = \rho(r, \varphi, z), \\ \langle \mathbf{B}^W - \mathbf{B}^I \rangle \cdot \vec{e}_r = 0. \end{cases} \tag{4.6}$$

two-scale asymptotic expansions

As we are interested in subwavelength behavior, $d \ll \lambda$, we expand $\mathbf{E}^W, \mathbf{B}^W; \mathbf{E}^I, \mathbf{B}^I$ in the two-scale expansion

$$\begin{cases} \mathbf{E}^W &= (\mathbf{E}^{W0}(y, z, r, \varphi) + d\mathbf{E}^{W1}(y, z, r, \varphi) + O(|d^2|))e^{i\omega t}, \\ \mathbf{B}^W &= (\mathbf{B}^{W0}(y, z, r, \varphi) + d\mathbf{B}^{W1}(y, z, r, \varphi) + O(|d^2|))e^{i\omega t}, \\ \mathbf{E}^I &= (\mathbf{E}^{I0}(y, z, r, \varphi) + d\mathbf{E}^{I1}(y, z, r, \varphi) + O(|d^2|))e^{i\omega t}, \\ \mathbf{B}^I &= (\mathbf{B}^{I0}(y, z, r, \varphi) + d\mathbf{B}^{I1}(y, z, r, \varphi) + O(|d^2|))e^{i\omega t}. \end{cases} \tag{4.7}$$

We substitute the series 4.7 into Maxwell's equations 4.2, 4.3, perfect conducting boundary conditions 4.4 and transmission conditions 4.6 to recover the leading order theory describing propagating fields inside the waveguide. An outline of the derivation is provided in 5.6 . In the following, components of the electric and magnetic fields are written in cylindrical coordinates using the convention $\mathbf{E}^{W0} = (E_r^{W0}, E_z^{W0}, E_\varphi^{W0})$, $\mathbf{B}^{I0} = (B_r^{I0}, B_z^{I0}, B_\varphi^{I0})$, etc.

leading order theory: the subwavelength limit of the asymptotic expansions

We present the boundary value problem for $\mathbf{E}^{W0}$, $\mathbf{B}^{W0}$, $\mathbf{E}^{I0}$, $\mathbf{B}^{I0}$. The derivation is given in the Appendix 5.6. In the interior waveguide, $0 < r < r_m$, the leading order fields $\mathbf{E}^{W0}, \mathbf{B}^{W0}$ are independent of the y variable, depending only on r, φ, z and are solutions Maxwell's equations

$$\begin{cases} \nabla\times\mathbf{E}^{W0} &= -i\omega\mathbf{B}^{W0}, \\ \nabla\times\mathbf{B}^{W0} &= i\omega\mu_0\epsilon_0\mathbf{E}^{W0}, \\ \nabla\cdot\mathbf{B}^{W0} &= 0, \\ \nabla\cdot\mathbf{E}^{W0} &= 0. \end{cases} \tag{4.8}$$

Inside the impedance layer, $r_m < r < r_m + h$, the fields $\mathbf{E}^{I0}, \mathbf{B}^{I0}$ have the form

$$\begin{cases} \mathbf{E}^{I0} &= \vec{e}_z E_z^{I0}, \\ \mathbf{B}^{I0} &= \vec{e}_\varphi B_\varphi^{I0} + \vec{e}_r B_r^{I0}, \end{cases} \tag{4.9}$$

and E_z^{I0}, B_φ^{I0}, B_r^{I0} are functions of r, φ, z. At the interface, $r = r_m$,

$$\begin{aligned} E_\varphi^{W0} &= 0, & E_z^{W0} &= E_z^{I0}, \\ -(B_\varphi^{W0} - \theta(r_m)B_\varphi^{I0}) &= J_z, & B_z^{W0} &= J_\varphi, \\ \epsilon_0 E_r^{W0} &= \rho, & B_r^{W0} &= B_r^{I0}, \end{aligned} \tag{4.10}$$

where ρ, J_z and J_φ are surface charge densities and currents. At $r = r_m + h$,

$$B_r^{I0}(z, r_m + h, \varphi) = 0, \qquad E_z^{I0}(z, r_m + h, \varphi) = 0. \tag{4.11}$$

Here E_z^{I0}, B_φ^{I0}, B_r^{I0} satisfy the system

$$\frac{1}{r}\partial_r\left(\frac{r}{\theta(r)}\partial_r(\theta E_z^{I0})\right) + \frac{1}{r}\left(\frac{1}{r}\partial_\varphi E_z^{I0}\right) = -\omega^2\mu_0\epsilon_0 E_z^{I0}, \tag{4.12}$$

$$E_z^{I0}(z, r_m + h, \varphi) = 0, \tag{4.13}$$

$$B_r^{I0}(z, r_m + h, \varphi) = 0, \tag{4.14}$$

$$B_r^{I0} = -\frac{1}{i\omega}\frac{1}{r}\partial_\varphi E_z^{I0}, \tag{4.15}$$

$$B_\varphi^{I0} = \frac{1}{i\omega\theta}\partial_r(\theta E_z^{I0}), \tag{4.16}$$

where equation 4.14 follows immediately from 4.15, noting that $\partial_\varphi E_z^{I0}$ is the tangential derivative on $r = r_m + h$ of E_z^{I0} and $E_z^{I0} = 0$ on $r = r_m + h$.

Taken together, equations 4.8 - 4.16 provide transmission and boundary conditions satisfied by $\mathbf{E}^{W0}$ and $\mathbf{B}^{W0}$ over the inner waveguide Ω_W. In the next section we apply these equations to characterize the solutions of a transmission boundary value problem for which the surface current J_z defined by 4.10 vanishes and rewrite this problem as one posed exclusively over Ω_W with an effective surface impedance boundary condition given on $r = r_m$.

nonlocal surface impedance formulation for time harmonic fields

We make the ansatz $J_z = 0$. With this ansatz we get $B_\varphi^{W0} = \theta(r_m)B_\varphi^{I0}$ and reinterpret the leading order theory for the time-harmonic electric and magnetic fields $\mathbf{E}^{W0}$ and $\mathbf{B}^{W0}$ as a problem defined on the circular waveguide Ω_W but now equipped with a nonlocal anisotropic surface impedance.

In the domain $0 < r < r_m$, we have that the zero-order fields $\mathbf{E}^{W0}, \mathbf{B}^{W0}$ satisfy Maxwell's equations 4.8. Now we introduce the Dirichlet to Neumann map at the

interface $r = r_m$. Define $F(r,\varphi)\vec{e}_z$ taking prescribed boundary data $f(\varphi)$ at $r = r_m$ and satisfying $F(r_m + h, \varphi) = 0$ and

$$\frac{1}{r}\partial_r\left(\frac{r}{\theta(r)}\partial_r(\theta(r)F)\right) + \frac{1}{r}\partial_\varphi\left(\frac{1}{r}\partial_\varphi F\right) = -\omega^2\mu_0\epsilon_0 F \tag{4.17}$$

on $r_m < r < r_m + h$, $0 \le \varphi \le 2\pi$.

The Dirichlet to Neumann map for this problem, denoted by $\mathcal{N}_{\varphi,z}$, maps the Dirichlet data $F(r_m,\varphi) = f(\varphi)\vec{e}_z$ to the Neumann data $\frac{1}{i\omega}\partial_r(\theta F)_{|r_m}\vec{e}_\varphi$. At the interface $r = r_m$, we impose 4.10 together with 4.12 and 4.13 to see that the anisotropic nonlocal surface impedance conditions are given on $r = r_m$ by

$$E_\varphi^{W0}(r_m,\varphi,z) = 0, \qquad B_\varphi^{W0}(r_m,\varphi,z) = \mathcal{N}_{\varphi,z}E_z^{W0}(r_m,\varphi,z). \tag{4.18}$$

Collecting results we obtain our fundamental result.

Proposition 4.1. Periodic Corrugations as Metamaterials.

In the subwavelength limit $d \to 0$, a solution to the homogenized problem is given by the solution $(\mathbf{E}^{W0}, \mathbf{B}^{W0})$ of the time-harmonic Maxwell's equations 4.8 in the circular waveguide Ω_W that satisfies the nonlocal anisotropic surface impedance conditions on the circular boundary $r = r_m$ of Ω_W given by 4.18.

In the next section we apply this result to hybrid waveguide modes and recover a homogenized problem posed in terms of an effective surface impedance.

effective surface impedance for hybrid modes in circular waveguides

In this section we apply Proposition 4.1 to recover the leading order theory for waveguide modes inside the circular cylindrical waveguide. Waveguide modes inside the circular waveguide Ω_W have electric and magnetic fields according the following separated forms, see [9], [15]. In the interior waveguide, we have electric field

$$\mathbf{E}^{W0} = R_z^{En}(r)T_z^{En}(\varphi)e^{-i\beta z}\vec{e}_z + R_\varphi^{En}(r)T_\varphi^{En}(\varphi)e^{-i\beta z}\vec{e}_\varphi + R_r^{En}(r)T_r^{En}(\varphi)e^{-i\beta z}\vec{e}_r \tag{4.19}$$

and magnetic field

$$\mathbf{B}^{W0} = R_z^{Bn}(r)T_z^{Bn}(\varphi)e^{-i\beta z}\vec{e}_z + R_\varphi^{Bn}(r)T_\varphi^{Bn}(\varphi)e^{-i\beta z}\vec{e}_\varphi + R_r^{Bn}(r)T_r^{Bn}(\varphi)e^{-i\beta z}\vec{e}_r \quad (4.20)$$

where the propagation constant $\beta = \frac{2\pi}{\lambda}$ and $n = 0, 1, 2, \ldots$. Here all functions $T(\varphi)$ of φ are of the form

$$T(\varphi) = a_n e^{in\varphi}, \quad (4.21)$$

where a_n is an arbitrary complex constant. We write $F(r, \varphi) = R(r)T(\varphi)$ and substitution of this form into 4.17 shows that $R(r)$ is the solution of

$$\begin{cases} r\partial_r\left(\frac{r}{\theta(r)}\partial_r(\theta(r)R(r))\right) + (k^2 - n^2)\,R(r) = 0,\ r_m < r < r_m + h, \\ R(r_m) = 1, \\ R(r_m + h) = 0, \end{cases} \quad (4.22)$$

where $k^2 = \omega^2/c^2$, $c = 1/\sqrt{\mu_0\epsilon_0}$ and μ_0 and ϵ_0 are the magnetic permeability and dielectric permittivity of the vacuum. From 4.18 we recover the anisotropic effective surface impedance conditions given by

$$E_\varphi^{W0}(r_m, \varphi, z) = 0, \qquad B_\varphi^{W0}(r_m, \varphi, z) = \mu_0\mathcal{Y}_{ad}E_z^{W0}(r_m, \varphi, z). \quad (4.23)$$

Here the surface impedance is expressed in terms of the effective admittance $\mathcal{Y}_{ad}$ given by

$$\mathcal{Y}_{ad}(k, n) = \frac{y_0}{ik}\partial_r(\theta(r)R(r))\Big|_{r=r_m}, \quad (4.24)$$

where $y_0 = \epsilon_0/\mu_0$ is the free space admittance. Collecting results we find that subwavelength dispersion inside corrugated metallic waveguides is given to leading order by replacing the highly oscillatory corrugated boundary with a metamaterial having an anisotropic surface impedance.

Proposition 4.2. Periodic Corrugations as Metamaterials II.

In the subwavelength limit $d \to 0$ all hybrid modes $(\mathbf{E}^{W0}, \mathbf{B}^{W0})$ are given by

$$\begin{cases} E_z^{W0} = a_n J_n(x) e^{i(n\varphi - \beta z)}, \\ E_r^{W0} = -a_n i \frac{k}{K} \frac{J_n(x)}{x} \{\overline{\beta} F_n(x) + n\overline{\Lambda}\} e^{i(n\varphi - \beta z)}, \\ E_\varphi^{W0} = a_n \frac{k}{K} \frac{J_n(x)}{x} \{n\overline{\beta} + \overline{\Lambda} F_n(x)\} e^{i(n\varphi - \beta z)}, \\ B_z^{W0} = -a_n c^{-1} \overline{\Lambda} J_n(x) e^{i(n\varphi - \beta z)}, \\ B_r^{W0} - a_n \frac{k}{K} c^{-1} \frac{J_n(x)}{x} \{\overline{\beta\Lambda} F_n(x) + n\} e^{i(n\varphi - \beta z)}, \\ B_\varphi^{W0} = -a_n i \frac{k}{K} c^{-1} \frac{J_n(x)}{x} \{n\overline{\beta\Lambda} + F_n(x)\} e^{i(n\varphi - \beta z)}, \ n = 0, 1, \ldots, \end{cases} \tag{4.25}$$

where J_n is the Bessel function of order n, $x = Kr$, $K^2 = k^2 - \beta^2$, $\overline{\beta} = \beta/k$, $F_n(x) = xJ_n'(x)/J_n(x)$, and the mode coupling parameter $\overline{\Lambda}$ is given by $-ic^{-1}\overline{\Lambda} = B_z^{WO}/E_z^{WO}$. All modes satisfy the anisotropic surface impedance conditions on the circular boundary $r = r_m$ of Ω_W given by 4.23 and $\mathcal{Y}_{ad}$ given by 4.24. The condition $E_\varphi^{W0}(r_m, \varphi, z) = 0$ specifies the coupling constant, and for $x_m = Kr_m$ is given by

$$n\overline{\beta} + \overline{\Lambda} F_n(x_m) = 0. \tag{4.26}$$

The condition $B_\varphi^{W0}(r_m, \varphi, z) = \mu_0 \mathcal{Y}_{ad} E_z^{W0}(r_m, \varphi, z)$ provides the k versus β dispersion relation for the waveguide modes given by

$$\mu_0 \mathcal{Y}_{ad}(k, n) = -i \frac{k}{x_m K} \{n\overline{\beta\Lambda} + F_n(x_m)\}. \tag{4.27}$$

For general corrugation shapes specified by $\theta(r)$ the admittance $\mathcal{Y}_{ad}(k, n)$ is computed through the numerical solution of 4.22. The dispersion relation is then solved for β at fixed k using a root finder in 4.27. For rectangular profiles $\theta(r)$ is a constant, 4.22 is a boundary value problem for Bessel's equation, and direct solution of 4.22 gives the explicit formula for the admittance

$$\mathcal{Y}_{ad}(k, n) = -i \frac{\theta(r_m)}{c} \frac{Y_n(k(r_m + h)) J_n'(kr_m) - J_n(k(r_m + h)) Y_n'(kr_m)}{Y_n(k(r_m + h)) J_n(kr_m) - J_n(k(r_m + h)) Y_n(kr_m)}. \tag{4.28}$$

This formula shows that the effective admittance depends linearly on the relative width of the corrugation as well as its depth h. For $\theta = 1$, formula 4.28 recovers the surface impedance formula for corrugated waveguides with infinitely thin ribs postulated in the early 1970's by Clarricoats and Saha [9]. This provides the connection between the metamaterial concept and the surface impedance formalism developed in the mid 20^{th} century microwave literature.

We apply equation 4.27 to examine the effect of corrugation depth and shape on dispersion curves in section 4.5.

4.4 metamaterials and corrugations as micro resonators

The characteristic feature of metamaterials is the coupling of macroscopic fields through structurally generated subwavelength resonance. For artificial magnetism generated in bulk metamaterials this is accomplished using split ring resonators made from perfect conductors as in [7]. For the metallic corrugated waveguides treated here, it is the finely spaced corrugations that function as micro resonators and provide the artificial magnetic coupling between macroscopic electric and magnetic fields. Here the coupling is through the frequency-dependent effective surface admittance $\mathcal{Y}_{ad}$. The resonances of the surface admittance at a fixed frequency depend upon the depth of the corrugations. Here depth is measured in relative units as the ratio $r_m/(r_m + h)$, where smaller ratios correspond to deeper corrugations. This is illustrated in Figures 4.6a and 4.6b for square corrugations and truncated sinusoidal profiles, were the truncated sinusoidal profiles have the form

$$\theta(r) = \frac{1}{2} + \frac{1}{\pi}\arcsin[2(r - (r_m + h/2))/1.2h].$$

The admittance is plotted as a function of frequency for fixed corrugation depth for both square and truncated sinusoidal profiles in Figures 4.7a to 4.9. It is seen

that the admittance changes sign and exhibits resonances at different frequencies for different corrugation profiles.

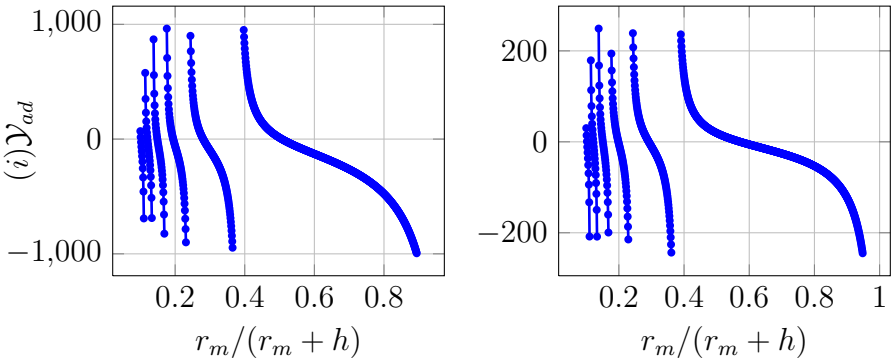

(a) (b)

FIGURE 4.6. Admittance $\mathcal{Y}_{ad}$ as a function of corrugation depth ratio $r_m/(r_m+h)$ for (a) square ribbed corrugations ($\theta \equiv 3/5$) and (b) truncated sinusoidal corrugations at fixed frequency $\omega \approx 50 \times 10^9$ rad/s, which corresponds to $kr_m = 2.0$

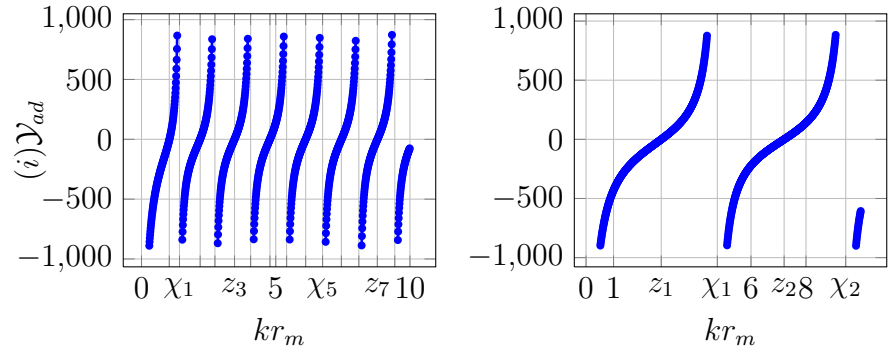

(a) $r_m/(r_m+h) = 0.30$ (b) $r_m/(r_m+h) = 0.60$

FIGURE 4.7. (a) Admittance $\mathcal{Y}_{ad}$ as a function of frequency for fixed ratio $r_m/(r_m+h) = 0.30$ with square ribbed corrugations ($\theta \equiv 3/5$). Resonances are seen at frequencies where kr_m takes values of $\chi_1 \approx 1.415$, $\chi_2 \approx 2.735$, $\chi_3 \approx 4.065$, $\chi_4 \approx 5.405$, $\chi_5 \approx 6.745$, $\chi_6 \approx 8.095$, $\chi_7 \approx 9.435$. Zeros are seen at $z_1 \approx 1.035$, $z_2 \approx 2.185$, $z_3 \approx 3.465$, $z_4 \approx 4.785$, $z_5 \approx 6.115$, $z_6 \approx 7.445$, $z_7 \approx 8.785$. (b) Admittance $\mathcal{Y}_{ad}$ as a function of frequency for fixed ratio $r_m/(r_m+h) = 0.60$ with square ribbed corrugations ($\theta \equiv 3/5$). Resonances are seen at frequencies where kr_m takes values of $\chi_1 \approx 4.775$, $\chi_2 \approx 9.445$. Zeros are seen at $z_1 \approx 2.735$, $z_2 \approx 7.205$.

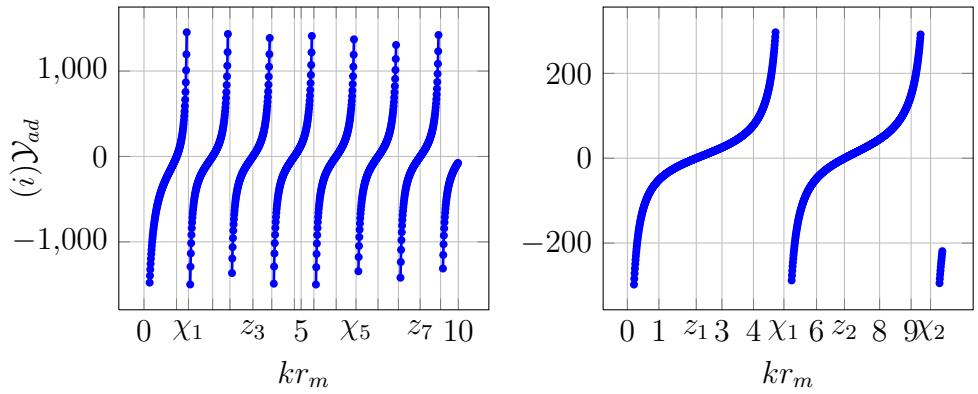

(a) $r_m/(r_m + h) = 0.30$ (b) $r_m/(r_m + h) = 0.60$

FIGURE 4.8. (a) Admittance $\mathcal{Y}_{ad}$ as a function of frequency for fixed ratio $r_m/(r_m + h) = 0.30$ with truncated sinusoidal corrugations. Resonances are seen at frequencies where kr_m takes values of $\chi_1 \approx 1.415$, $\chi_2 \approx 2.735$, $\chi_3 \approx 4.065$, $\chi_4 \approx 5.405$, $\chi_5 \approx 6.745$, $\chi_6 \approx 8.095$, $\chi_7 \approx 9.435$. Zeros are seen at $z_1 \approx 1.035$, $z_2 \approx 2.185$, $z_3 \approx 3.465$, $z_4 \approx 4.785$, $z_5 \approx 6.115$, $z_6 \approx 7.445$, $z_7 \approx 8.785$. (b) Admittance $\mathcal{Y}_{ad}$ as a function of frequency for fixed ratio $r_m/(r_m + h) = 0.60$ with truncated sinusoidal corrugations. Resonances are seen at frequencies where kr_m takes values of $\chi_1 \approx 4.965$, $\chi_2 \approx 9.615$. Zeros are seen at $z_1 \approx 2.185$, $z_2 \approx 6.885$.

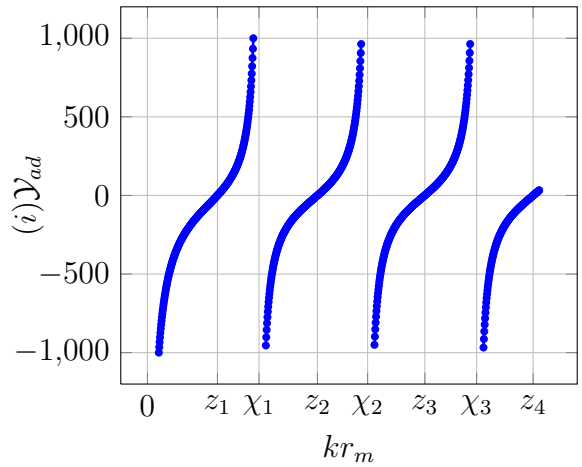

FIGURE 4.9. Admittance $\mathcal{Y}_{ad}$ as a function of frequency for the rectangular corrugations ($\theta \equiv 1/2$) considered in [12]. r_m =1.6 cm, and h =1.8 cm (this corresponds to depth ratio $r_m/(r_m + h) = 0.4706$). Resonances are seen at frequencies where kr_m takes values of $\chi_1 \approx 2.845$, $\chi_2 \approx 5.615$, $\chi_3 \approx 8.395$. Zeros are seen at $z_1 \approx 1.785$, $z_2 \approx 4.335$, $z_3 \approx 7.075$, $z_4 \approx 9.835$.

4.5 controlling negative dispersion and power flow with corrugation depth

Backward waves are traveling wave modes with group velocity and phase velocity in opposing directions. In all cases the phase velocity is directed along the waveguide in the positive $\vec{e_z}$ direction. In this section we show existence of backward waves for corrugated waveguides when the corrugations are sufficiently deep. It is seen that group velocity and integrated power flow can be made opposite the phase velocity, depending on the depth of the corrugations. We also confirm that negative group velocity modes correspond to EH_{11} modes defined by $E_z > H_z$. This is important to describe Cherenkov interaction between the electromagnetic wave and electrons inside traveling wave tube amplifiers [12].

Figures 4.10a to 4.11b give dispersion curves for hybrid modes and their dependence on the depth of corrugations. As before depth is measured in relative units as the ratio $r_m/(r_m + h)$ and we consider corrugation depths associated with ratios between 0.3 and 0.6. The dispersion relations are displayed in terms of normalized frequency and wave number given by kr_m and βr_m, respectively. For all cases we discover that there is a corrugation ratio below which all hybrid modes have backward waves associated with EH_{11} modes corresponding to $E_z > H_z$.

As a first example we consider square corrugations of relative width $\theta(r_m) = 3/5$. Figure 4.10a shows a bifurcation between forward and backward wave modes for corrugation depth between the ratios of 0.6 and 0.48. The cut on frequency for these modes is approximately 1.8 in normalized units. The dispersion relation for the 0.48 corrugation exhibits negative group velocity at cut on, while the mode associated with the 0.6 corrugation exhibits positive group velocity. The wave modes associated with deeper corrugations of ratios 0.4, 0.35, 0.3 are all EH_{11} modes and are backward waves exhibiting negative group velocity. For corrugations given

by truncated sinusoidal profiles Figure 4.10b shows similar trends. As seen before, there is a bifurcation between forward and backward wave modes for corrugation depth between the ratios of 0.6 and 0.48. The cut on frequency for these modes is roughly 1.8 for the backward wave and 1.9 for the forward wave. As before, the dispersion relation for the 0.48 corrugation exhibits negative group velocity at cut on, while the mode associated with the 0.6 corrugation exhibits positive group velocity. The wave modes associated with deeper corrugations of ratios 0.4, 0.35, 0.3 are also EH_{11} modes and are backward waves exhibiting negative group velocity. These trends are repeated for truncated sawtooth corrugations in Figure 4.11a and for the infinitely thin ribbed corrugations in Figure 4.11b. We conclude by plotting dispersion relations for the square corrugation geometries considered in [12], see Figure 4.12a. For this case, $r_m = 1.6$ cm, and we plot dispersion curves for ratios $r_m/(r_m + h)$ associated with different corrugation depths h. As before, we see a similar bifurcation between forward and backward modes in corrugated waveguides with increasing corrugation depth. We confirm existence of a backward wave EH_{11} mode at cut on for a corrugation depth of 1.8 cm. In Figure 4.12b we plot both normalized group velocity $(dk/d\beta)/c$ and integrated Poynting vector $\int_0^{r_m} \mathrm{d}P(r)$ for the square corrugations of [12], see 4.12a, with corrugation depth $h = 1.8$ cm. We see that both are negative at the cut on frequency and become positive for normalized wave numbers larger than 2.7. For comparison, we display Figure 4.13 associated with a positive wave for a square corrugation with $\theta(r_m) = 3/5$ and a corrugation depth of ratio 0.6. Here both normalized group velocity and integrated Poynting vector are positive for all wave numbers on the dispersion curve.

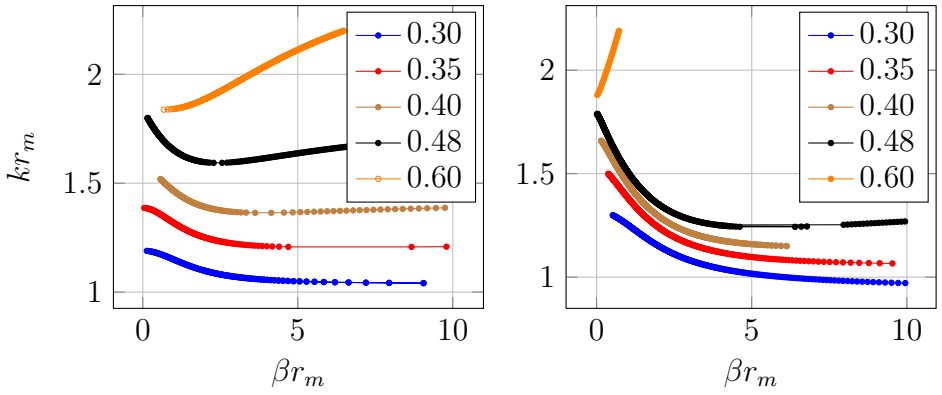

FIGURE 4.10. (a) Dispersion curves for square corrugations with $\theta \equiv 3/5$ for corrugation depth ratios $r_m/(r_m + h)$ in the range 0.3 to 0.6. (b) Dispersion curves for truncated sinusoidal corrugations having the form $\theta(r) = \frac{1}{2} + \frac{1}{\pi}\arcsin[2(r - (r_m + h/2))/1.2h]$ for corrugation depth ratios $r_m/(r_m + h)$ in the range 0.3 to 0.6.

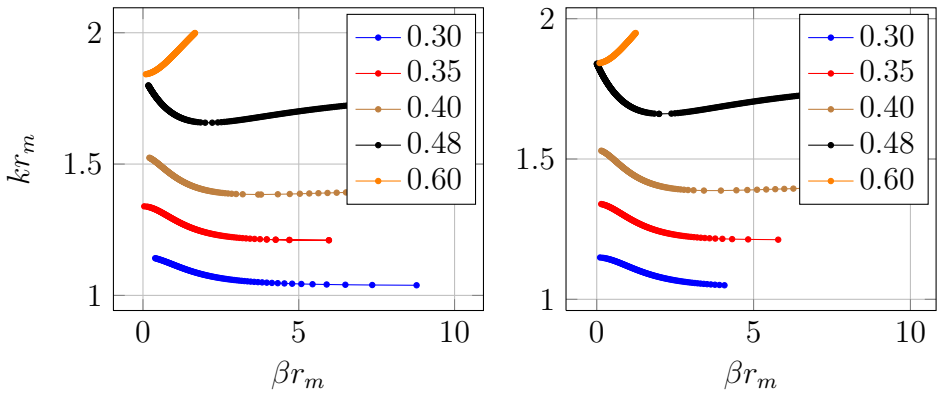

FIGURE 4.11. (a) Dispersion curves for truncated sawtooth corrugations. The profile function $\theta(r)$ decreases linearly from $\theta(r_m) = d_1 = 3.175$ mm to $\theta(r_m + h) = d_2$ mm. The slope of this profile then depends on the corrugation depth h. The profile function is given by $\theta(r) = d_1 + ((d_2 - d_1)/h)(r - r_m)$. These are plotted for for corrugation depth ratios $r_m/(r_m + h)$ in the range 0.3 to 0.6. (b) Dispersion curves for infinitely thin ribbed corrugations for corrugation depth ratios $r_m/(r_m + h)$ in the range 0.3 to 0.6.

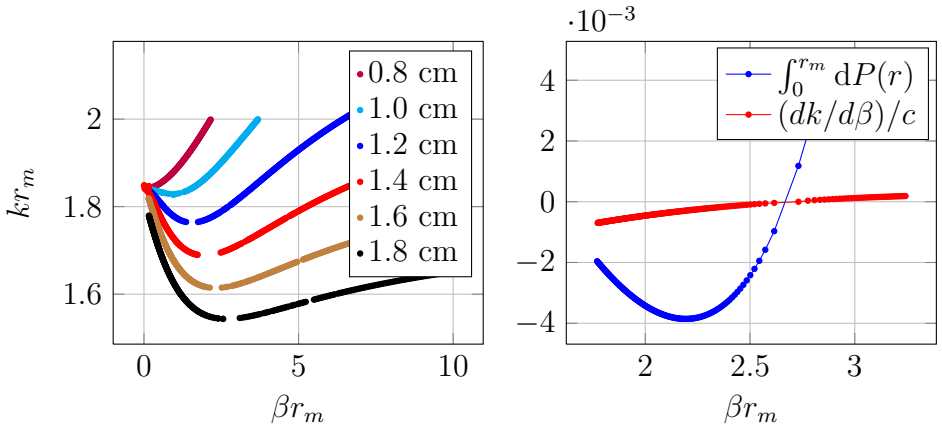

(a) (b)

FIGURE 4.12. (a) Dispersion relation for the square corrugations considered in [12]. Here an inner waveguide of radius $r_m = 1.6$ cm with square ribbed corrugations ($\theta \equiv 1/2$). Dispesrion relations are given for depths $h = 0.8$ cm ($r_m/(r_m + h) \approx 0.667$), 1.0 cm ($r_m/(r_m + h) \approx 0.615$),1.2 cm ($r_m/(r_m + h) \approx 0.5714$), 1.4 cm ($r_m/(r_m + h) \approx 0.5333$), 1.6 cm ($r_m/(r_m+h) = 0.5$), 1.8 cm ($r_m/(r_m+h) \approx 0.4706$). (b) Normalized group velocity $(dk/d\beta)/c$ and integrated Poynting vector $\int_0^{r_m} \mathrm{d}P(r)$ for the square corrugations of [12], see 4.12a, with corrugation depth $h = 1.8$ cm (a ratio of $r_m/(r_m + h) = 0.4706$).

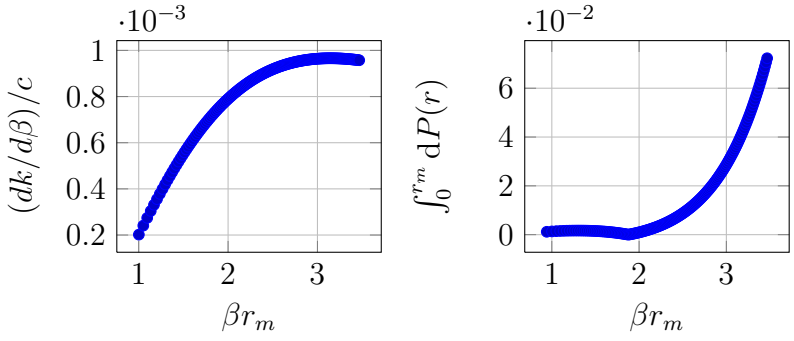

(a) Normalized group velocity (b) Integrated Poynting vector

FIGURE 4.13. Normalized group velocity $(dk/d\beta)/c$ and integrated Poynting vector $\int_0^{r_m} \mathrm{d}P(r)$ for the square corrugations ($\theta \equiv 3/5$; see 4.10a) with corrugation ratio $r_m/(r_m + h) = 0.6$. We observe that both the group velocity and the power flow are positive.

4.6 conclusions

We have applied two-scale asymptotic expansions to confirm that negative group velocity can be induced through the design of subwavelength corrugations that are sufficiently deep. Our analysis and simulations definitively show that this phenomenon occurs due to the coupling of macroscopic electric and magnetic fields through subwavelength resonance. This is manifested in an anisotropic effective surface impedance coupling electric to magnetic fields. The theory shows it is possible to represent corrugated waveguides as smooth cylindrical waveguides with a metamaterial surface characterized by an effective surface admittance. The effective surface admittance is the Dirichlet to Neumann map for a two point boundary value problem in terms of an ordinary differential equation with coefficients that depend on the corrugation shape. The interval over which the boundary value problem is posed depends upon the corrugation depth h and corresponds to the interval $r_m < r < r_m + h$. The reduced order model is far faster to compute than direct numerical simulation and can be used as a design tool for dispersion engineering. The reduced model allows one to quickly traverse the universe of geometries associated with corrugation profiles and depths enabling fast prototyping of slow wave interaction structures for use in Cherenkov Masers [5].

Chapter 5
Reduced Order Model for Amplifier

5.1 introduction

Motivation for developing the model for an amplifier and its mathematical theory is discussed in section.1.3. Traveling wave tube amplifier consists of a cylindrical dielectrically loaded waveguide with an electron beam running through its center. The strong uniform magnetic field applied along the beam confines election propagation to the center. Vacuum separates the beam from the surrounded cylindrical dielectric jacket. Amplification is possible in a traveling wave tube (TWT) provided its dielectric constant is larger than unity [5],[19]. In high power regime, most dielectric materials get ionized and breaks down after a few cycles of operation. In [16] Shiffler et al., propose all-metal dielectric constant greater than unity as an interaction structure. We use this in formulating our models. We answer the question of how a metal interaction structure affects tuneability of gain, bandwidth, and cut-on frequency for a TWT amplifiers. Amplifier increases the magnitude of the wave form as the wave travel down the TWT. Our zero-order problem recovers the dispersion curves of our collaborators for the cold structure.

5.2 background, motivation, and main results

Our work is motivated by the need to have an alternative to the transmission line model for beam-wave interaction in the high power regime. Transmission Line Model was exploited in [20] for a rounded rectangle and ellipsoidal geometries in cylindrical waveguides and many others. Its working principle is to characterize the effect of geometry of slow wave structure (SWS) on the transmission pattern and also on the gain and bandwidth. Here we depart from the earlier work and show that it is possible to characterize the influence of the geometry of the SWS

on the gain and bandwidth by asymptotic expansion of the Bloch wave in terms of δk and α.

5.3 amplifier model description

We consider a cylindrical waveguide of unit length with Floquet boundary conditions at $z = 0$ and $z = d$. The radius of the waveguide does not exceed $r_m + h = 2cm$, and the corrugation depth does not exceed h. Hence, the region of the SWS with periodic variation is contained in the annular domain $\{r \mid r_m \leq r \leq r_m + h\}$; see Figure 5.1. The longitudinal period of the corrugations is given by d. The entire

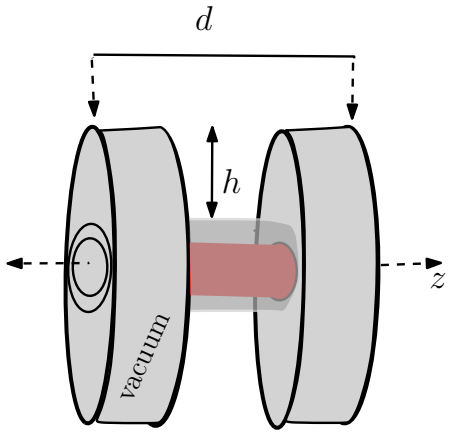

FIGURE 5.1. Square rib corrugations in domain $\{r \mid r_m \leq r \leq r_m + h\}$ of cylindrical waveguide

system is excited by a generator. Each of these components has different characteristic impedances, and reflections can occur at both input and output ends of the amplifier. The objective is to characterize the influence of the geometry of the interaction structure on the transmission pattern as well as its effect on the gain.

In this study, we employ d-periodic square ribbed [12] and misaligned elliptical [23] corrugations, see Figure 5.2. The corrugation shape is initially defined on a unit period, and corrugations are described on rescaling by d.

Within the waveguide, we assume a vacuum while the surrounding metallic wall is treated as a perfect conductor. Thus, the electric and magnetic fields in the

waveguide satisfy Maxwell's equations inside the corrugated wall, satisfy the conditions of a perfect conductor on the surface of the outer wall, and are zero within the thin conducting shell. Our asymptotic analysis results in a reduced model with periodic corrugations surface surrounding the inner waveguide region $\{r \mid r \leq r_m\}$. For general modes propagating in the waveguide, our effective reduced model is described in 5.3 below. The numeric results are discussed in 5.4.

physics of waveguides & **maxwell's equations**

The periodic corrugation is represented by rescaling a unit-periodic geometry (see Figure 5.2). The cylindrical waveguide has corrugated outer walls. We investigate square ribbed corrugation profiles [12] as well as misaligned elliptical corrugation [23], see Figure 5.2.

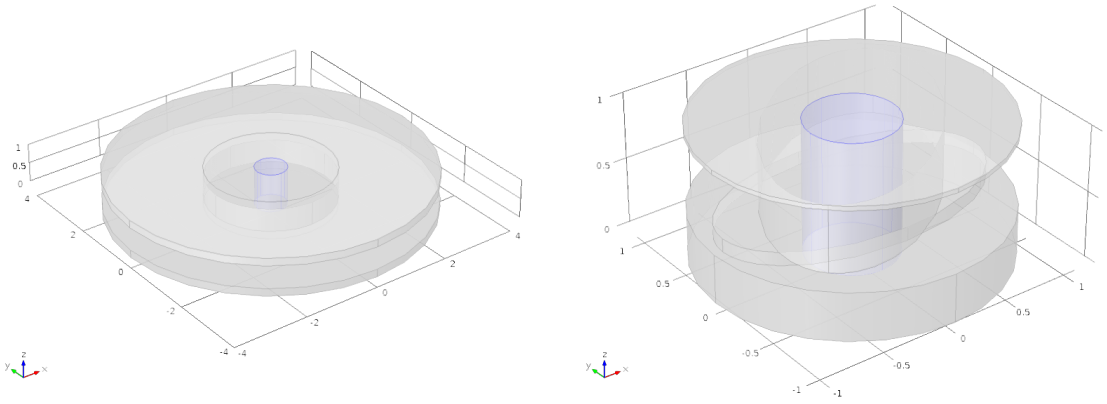

(a) (b)

FIGURE 5.2. Corrugation geometries considered: (a) square rib corrugations, (b) misaligned elliptical corrugations.

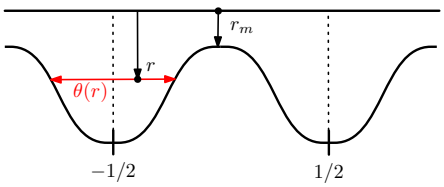

FIGURE 5.3. Unit-periodic geometry with d-periodic corrugation and profile function $\theta(r)$

We assume that the electric and magnetic fields within the waveguide have the form

$$\mathbf{E} = \mathbf{E}(z, r, \varphi)e^{-ikz}, \qquad \mathbf{B} = \mathbf{B}(z, r, \varphi)e^{-ikz}, \tag{5.1}$$

with $\mathbf{E}$ and $\mathbf{B}$ being d-periodic in z. Here, (z, r, φ) denote canonical cylindrical coordinates. $\mathbf{E}$ and $\mathbf{B}$ exhibit a d-periodic variation in z. Thus, the fields can be written as

$$\mathbf{E} = \mathbf{E}(z, r, \varphi)e^{-idkz}, \qquad \mathbf{B} = \mathbf{B}(z, r, \varphi)e^{-idkz}, \tag{5.2}$$

The waveguide is split into three concentric subdomains, denoted by Ω_W, Ω_I and Ω_b. Here, Ω_W is the cylindrical inner waveguide, $0 < r < r_m$; Ω_I is the cavity region interior to the waveguide domain, $r_m < r < r_m + h$ and Ω_b is the beam domain, $0 < r < R_b$ (see Figure 5.4).

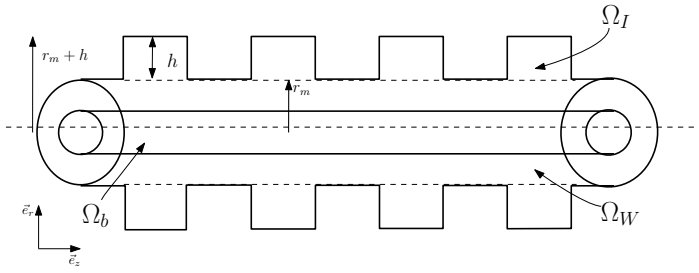

FIGURE 5.4. Domains Ω_W, Ω_I and Ω_b.

The fields inside Ω_W are denoted by $\mathbf{E}^W, \mathbf{B}^W$, and the fields inside Ω_I are denoted by $\mathbf{E}^I, \mathbf{B}^I$. As we assume e^{-idkz}-behavior, on Ω_W, fields $\mathbf{E}^W, \mathbf{B}^W$ solve Maxwell's equations

$$\begin{cases} \nabla \times \mathbf{E}^W = -i\omega \mathbf{B}^W, \\ \nabla \times \mathbf{B}^W = i\omega\mu_0\epsilon_0\epsilon_r \mathbf{E}^W, \\ \nabla \cdot \mathbf{B}^W = 0, \\ \nabla \cdot \mathbf{E}^W = 0, \end{cases} \tag{5.3}$$

and $\mathbf{E}^I, \mathbf{B}^I$ satisfy, on Ω_I,

$$\begin{cases} \nabla \times \mathbf{E}^I = -i\omega \mathbf{B}^I, \\ \nabla \times \mathbf{B}^I = i\omega \mu_0 \epsilon_0 \epsilon_r \mathbf{E}^I, \\ \nabla \cdot \mathbf{B}^I = 0, \\ \nabla \cdot \mathbf{E}^I = 0. \end{cases} \tag{5.4}$$

Considering ϵ_r is the same in both Ω_I and Ω_W. These equations can be represented with the $\nabla \times \nabla \times$ operator as one system in $\Omega = \Omega_I \cup \Omega_W \cup \Omega_b$,

$$\begin{cases} \nabla \times \epsilon^{-1}(r,z) \nabla \times \mathbf{B} = \frac{\omega^2}{c^2} \mathbf{B}, \\ \vec{\nu} \times \nabla \times \mathbf{B} = 0, \\ \nabla \cdot \mathbf{B} = 0. \end{cases} \tag{5.5}$$

On the outer boundary of the waveguide and at $z = 0$ and $z = 1$, denoting the unit outer normal vector field by $\vec{\nu}$, we impose perfect conducting boundary conditions

$$\vec{\nu} \times \nabla \times \mathbf{B} = 0, \qquad \mathbf{B} \cdot \vec{\nu} = 0. \tag{5.6}$$

and consider

$$\epsilon^{-1}(r,z) = \begin{cases} \vec{e}_r \otimes \vec{e}_r + \vec{e}_\theta \otimes \vec{e}_\theta + \vec{e}_z \otimes \vec{e}_z, \text{vacuum} \\ \vec{e}_r \otimes \vec{e}_r + \vec{e}_\theta \otimes \vec{e}_\theta + \vec{e}_z \otimes \vec{e}_z (1-\alpha)^{-1}, \text{beam} \end{cases} \tag{5.7}$$

The waveguide boundary can have flat parts. Here we recall that the boundary of the waveguide is a metallic shell given by a perfect conductor with zero electric and magnetic fields inside. With this in mind for $r = r_m$, we extend $\mathbf{B}^I$ by zero onto the flat parts. We write this observation as

$$\mathbf{B}(r_m, z, \varphi) = 0, \text{ for } y_-(r_m) < z < y_+(r_m). \tag{5.8}$$

We impose the following transmission conditions at $r = R_b$

$$[\vec{\nu} \times \epsilon(r,z)^{-1} \nabla \times \mathbf{B}]_{R_b^-}^{R_b^+} = 0, \qquad [\mathbf{B}]_{R_b^-}^{R_b^+} = 0 \tag{5.9}$$

non dimensional formulation

We can write the system 5.5 in dimensionless form by making the involved parameters and field dimensionless. So, $\mathbf{B}$ and ϵ in dimensionless form be written as $\epsilon(\frac{\tilde{x}}{d}) = \epsilon(\tilde{y})$ and $\mathbf{B}(\frac{\tilde{x}}{d}) = d^2\mathbf{V}(\tilde{y})$ and the parameters are represented as $\frac{\omega^2}{c^2} = \frac{d^2\omega^2}{c^2} = \beta^2$, $dk = \hat{\Omega}$.

asymptotic expansions

we expand $\mathbf{V}$ with $\hat{\Omega} = \hat{\Omega}_0 + \delta k$ and α.

$$\mathbf{V} = (\mathbf{V}^0(\tilde{y}) + \delta k\mathbf{V}^1(\tilde{y}) + \alpha\mathbf{V}^1(\tilde{y}) + o(\delta k, \alpha))e^{-i\delta k}, \tag{5.10}$$

We substitute the series 5.10 into Maxwell's equations 5.5, perfect conducting boundary conditions 5.6 and transmission conditions 5.9 to recover the leading order theory describing propagating fields inside the waveguide.

leading order theory: the subwavelength limit of the asymptotic expansions

We present the boundary value problem for $\mathbf{B}^0$. In the domain Ω, the leading order fields $\mathbf{B}^0$ depend on r, z and are solutions of Maxwell's equations

$$\begin{cases} \nabla \times \nabla \times \mathbf{V}^0 = \beta^2\mathbf{V}^0, & \Omega \\ \vec{\nu} \times \nabla \times \mathbf{V}^0 = 0, & \partial\Omega \\ \nabla \cdot \mathbf{V}^0 = 0, & \Omega \\ \mathbf{V}^0(y + e_z) = \mathbf{V}^0(y)e^{-i\hat{\Omega}_0} \end{cases} \tag{5.11}$$

Similarly, we derive the 1^{nd} order problem,

$$\begin{cases} \nabla \times \nabla \times \mathbf{V}^1 + \nabla \times (\mathbf{V}^0 \times ie_z) + (\nabla \times \mathbf{V}^0) \times ie_z = \beta^2\mathbf{V}^1, & \Omega \\ \vec{\nu} \times \nabla \times \mathbf{V}^1 + \vec{\nu} \times (\mathbf{V}^0 \times ie_z) = 0, & \partial\Omega \\ \nabla \cdot \mathbf{V}^1 = -i\mathbf{V}^0_z, & \Omega \\ \mathbf{V}^1(y + e_z) = \mathbf{V}^1(y)e^{-i\hat{\Omega}_0} \end{cases} \tag{5.12}$$

and 2^{rd} order problem, in $\Omega_V = \Omega_W \cup \Omega_I$

$$\begin{cases} \nabla \times \nabla \times \mathbf{V}^2 = \beta^2 \mathbf{V}^2, \\ \vec{\nu} \times \nabla \times \mathbf{V}^2 = 0, \\ \nabla \cdot \mathbf{V}^2 = 0. \end{cases} \tag{5.13}$$

& in Ω_b

$$\begin{cases} \nabla \times \nabla \times \mathbf{V}^2 + \nabla \times (\vec{e_z} \times \vec{e_z}) \nabla \times \mathbf{V}^0 = \beta^2 \mathbf{V}^2, \\ [\vec{\nu} \times \nabla \times \mathbf{V}^2]_{R_b^+}^{R_b^-} = -\vec{\nu} \times \vec{e_z} \otimes \vec{e_z} \nabla \times \mathbf{V}^0|_{R_b^-}, \\ \nabla \cdot \mathbf{V}^2 = 0. \end{cases} \tag{5.14}$$

dispersion relation for δk

Substitution of leading order terms into the variational formulation of Maxwell's equations for the TWT gives,

$$\begin{cases} \delta k [\int_\Omega \left((\nabla \times \mathbf{V}^0) \cdot \overline{(\nabla \times \mathbf{V}^1 + \mathbf{V}^0 \times i e_z)} + (\nabla \times \mathbf{V}^1 + \mathbf{V}^0 \times i e_z) \cdot \overline{(\nabla \times \mathbf{V}^0)} \right) dy \\ \qquad - \beta^2 \int_\Omega \left((\mathbf{V}^0 \cdot \overline{\mathbf{V}^1} + \mathbf{V}^1 \cdot \overline{\mathbf{V}^1}) \right) dy] \\ \qquad = \alpha [\beta^2 \int_\Omega \left((\mathbf{V}^0 \cdot \overline{\mathbf{V}^2} + \mathbf{V}^2 \cdot \overline{\mathbf{V}^0}) \right) dy \\ \qquad - \int_\Omega \left((\nabla \times \mathbf{V}^0) \cdot \overline{(\nabla \times \mathbf{V}^2)} + (\nabla \times \mathbf{V}^2) \cdot \overline{(\nabla \times \mathbf{V}^0)} \right) dy \\ \qquad - \int_{\Omega_b} (e_z \times e_z)(\nabla \times \mathbf{V}^0) \cdot \overline{(\nabla \times \mathbf{V}^0)} dy] \end{cases} \tag{5.15}$$

with $\alpha = \frac{{\omega_p}^2}{\gamma^3 \left(\frac{v_0}{d}\right)^2 \left(\left[\beta \frac{c}{v_0} - \hat{\Omega}_0 \right] - \delta k \right)^2}$, we get $\delta k = \alpha \frac{\mathbf{C}_2}{\mathbf{C}_1}$. Now plugging in α and after doing some algebra we have $\delta k \left(\left(\beta \frac{c}{v_0} - \hat{\Omega}_0 \right) - \delta k \right)^2 = \left(\frac{{\omega_p}^2}{\gamma^3 \left(\frac{v_0}{d}\right)^2} \right) \frac{\mathbf{C}_2}{\mathbf{C}_1}$, where $\Delta k = \left(\beta \frac{c}{v_0} - \hat{\Omega}_0 \right)$. Which allows one to recover the Pierce like equation for the perturbation

$$\delta k (\delta k - \Delta k)^2 = {K_0}^3 \tag{5.16}$$

where ${K_0}^3 = \left(\frac{{\omega_p}^2}{\gamma^3 \left(\frac{v_0}{d}\right)^2} \right) \frac{\mathbf{C}_2}{\mathbf{C}_1}$.This equation has one real root and two complex conjugate roots when $\Delta k + \frac{3}{4^{1/3}} K_0 > 0$. The gain per period is a function of $\mathrm{Im}\{\delta k\}$

given by 20log[exp(Im{δk} d)]. We are considering unit cell so, $d = 1$. Therefore 20log[exp(Im{δk})].

5.4 dispersion curve

We solve the cold structure problem 5.11 and study its dispersion curves by increasing the depth of the rib.

rib depth, ratio= 2.4

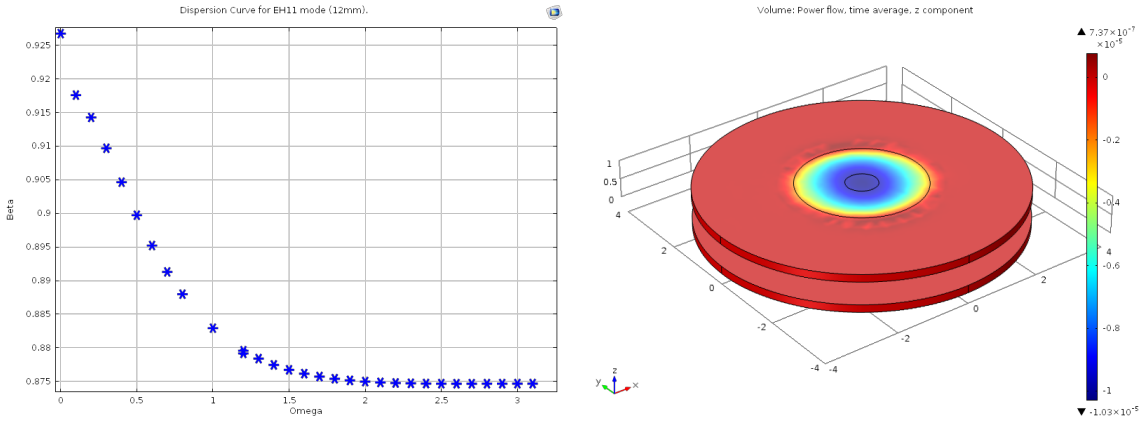

(a) (b)

FIGURE 5.5. ratio 2.4, depth ribbed: (a) Dispersion curve, (b) Power flow (z-component).

When we solve the unit periodic square ribbed cold structure problem 5.11 numerically by prescribing a propagation constant $\hat{\Omega}_0$, we get the hybrid mode with backward propagation as shown in Figure 5.5 (a), where the x-axis is the propagation constant $\hat{\Omega}_0$ and the y-axis is β. Figure 5.5 (b) shows the power flow on the negative scale, which means the power flow backward as we move along the dispersion curve.

rib depth, ratio= 2.8

We solve the cold structure problem 5.11 numerically by prescribing a propagation constant $\hat{\Omega}_0$. Results in the hybrid mode with backward propagation is shown in Figure 5.6 (a), where the x-axis is propagation constant $\hat{\Omega}_0$ and the y-axis is β. Figure 5.6 (b) shows the power flows backward as we move along the dispersion

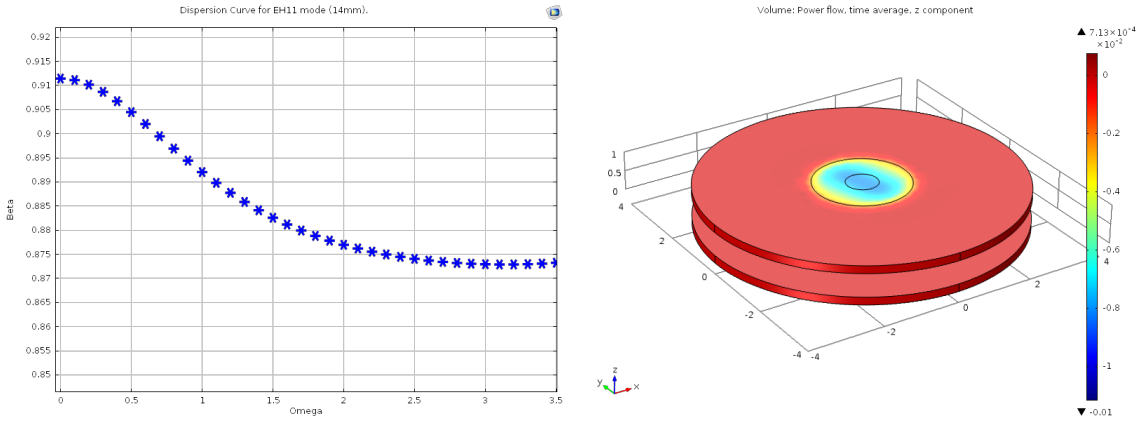

(a) (b)

FIGURE 5.6. ratio 2.8, depth ribbed: (a) Dispersion curve, (b) Power flow (z-component).

curve and its strength is greater as compared to 5.5 (b).

rib depth, ratio= 3.2

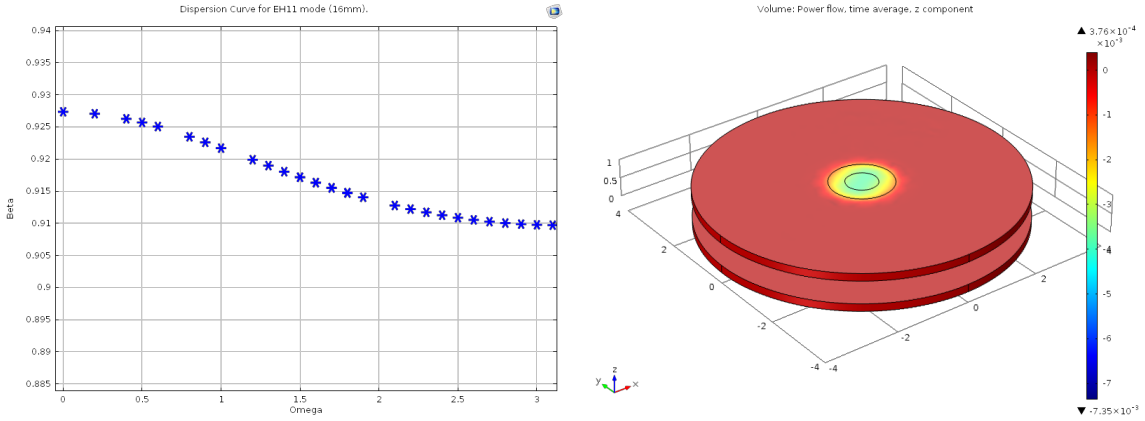

(a) (b)

FIGURE 5.7. ratio 3.2, depth ribbed: (a) Dispersion curve, (b) Power flow (z-component).

We get the hybrid mode with backward propagation as shown in Figure 5.7. When we prescribe a propagation constant $\hat{\Omega}_0$ and solve problem 5.11 numerically, where the x-axis is propagation constant $\hat{\Omega}_0$ and the y-axis is β. Figure 5.7 (b) shows the power flows backward as we move along the dispersion curve and its strength is greater as compared to both 5.5 (b) and 5.6 (b).

misaligned elliptical

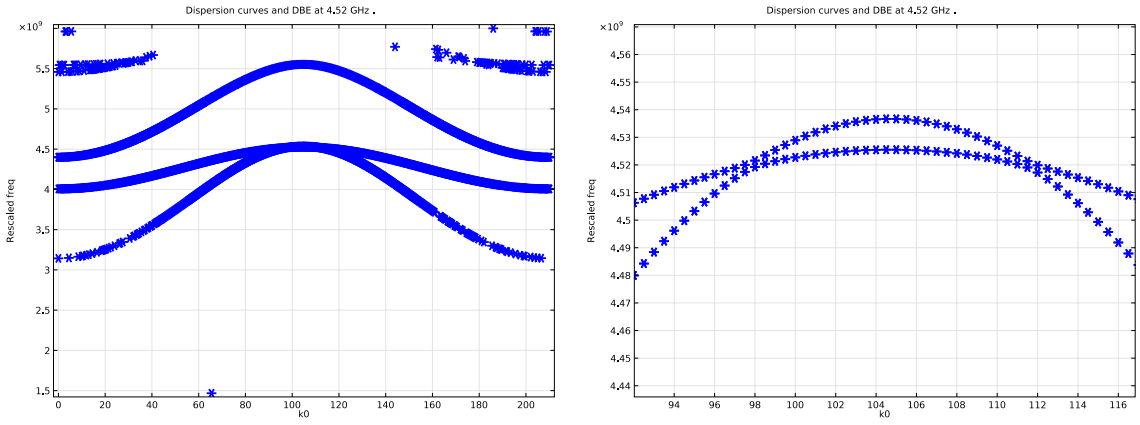

(a) (b)

FIGURE 5.8. (a) DBE dispersion curve, (b) Zoom at DBE.

When we solve the unit periodic cold structure problem 5.11 numerically by prescribing a propagation constant $\hat{\Omega}_0$ for the misaligned elliptical geometry interaction structure, we get the degenerate band edge (DBE) curve (see figure 5.8 (a)). It is called DBE because the forward propagating wave and the backward one meet and degenerate. The denerating point is shown in Figure 5.8 (b). The x-axis is the rescaled propagation constant $\hat{\Omega}_0$, which gives frequency in GHz and the y-axis is also the rescaled β, gives the wave number $(\frac{rad}{sec})$.

observation

When the depth of the rib is increased from ratio 2.4 to 3.2, the dispersion curve deepens. On further increase of the depths the curve starts getting flat. The reason for why the dispersion curve goes backward in propagation at a certain depth is explicitly explained in chapter 4 of this thesis. The strength of the z-component of the $\mathbf{V}^0$ fields increases as the depth increases from ratio 2.4 to 3.2.

5.5 gain factor per period curve

We solve 5.12 and 5.13 and 5.14 using the cold structure problem solution. Solutions are plugged into 5.15 for computing $\frac{C_2}{C_1}$ of the coupling wave number K_0. Finally, we calculate the gain factor for the SWS under investigation by finding the roots

of 5.16.

rib depth, ratio= 2.4

When we compute the gain per period by picking the points on the dispersion

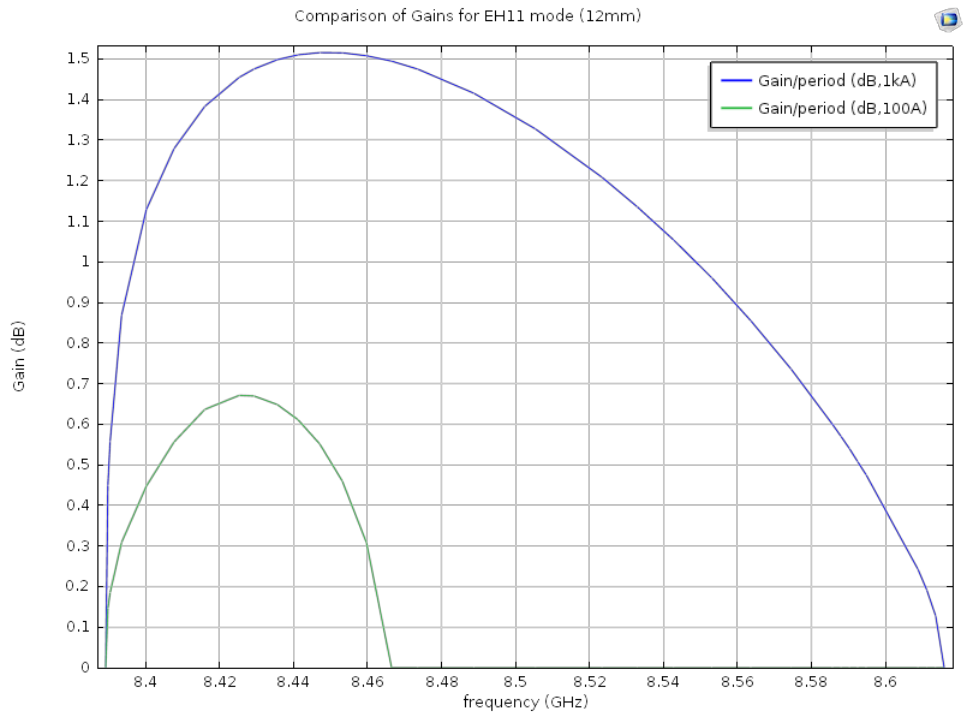

FIGURE 5.9. ratio 2.4, depth ribbed structure, gain per period curve

curve shown in Figure 5.5, we get the gain curve 5.9, which starts from zero and increases as one moves down the dispersion curve, attains a maximum at the slip Δk close to zero (see Table 5.1), then decreases to zero. In Figure 5.9, the x-axis is frequency in GHz and the y-axis is in decibels.

TABLE 5.1. Data at slip = 0.1256

	$I = 100$ A	$I = 1000$ A
ω_0 (rad/s)	5.3075×10^{10}	
f_0	8.4471 GHz	
Im$\{\delta k\}$	0.063451	0.17452
Gain factor	0.55113	1.5158
α	2.1853	5.5534
${K_0}^3$	0.00093909	0.0093909

rib depth, ratio= 2.8

When we compute the gain per period by picking the points on the dispersion

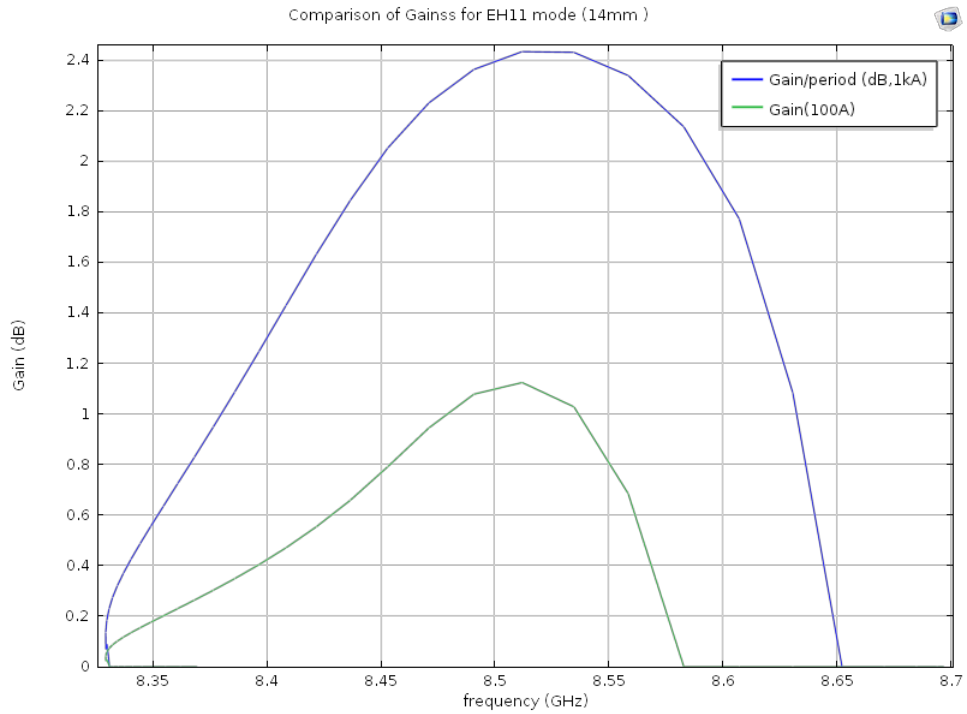

FIGURE 5.10. ratio 2.8, depth ribbed structure, gain per period curve

curve shown in Figure 5.6, we get the gain curve 5.10, which starts from zero and increases as one moves down the dispersion curve, attains a maximum at the slip Δk close to zero (see Table 5.2), then decreases to zero. In Figure 5.10, the x-axis is frequency in GHz and the y-axis is in decibels.

TABLE 5.2. Data at slip = 0.033488

	$I = 100$ A	$I = 1000$ A
ω_0 (rad/s)	5.3483×10^{10}	
f_0	8.5120 GHz	
Im$\{\delta k\}$	0.12943	0.28014
Gain factor	1.1242	2.4332
α	1.2183	2.7255
${K_0}^3$	0.0033488	0.033488

rib depth, ratio= 3.2

When we compute the gain per period by picking the points on the dispersion

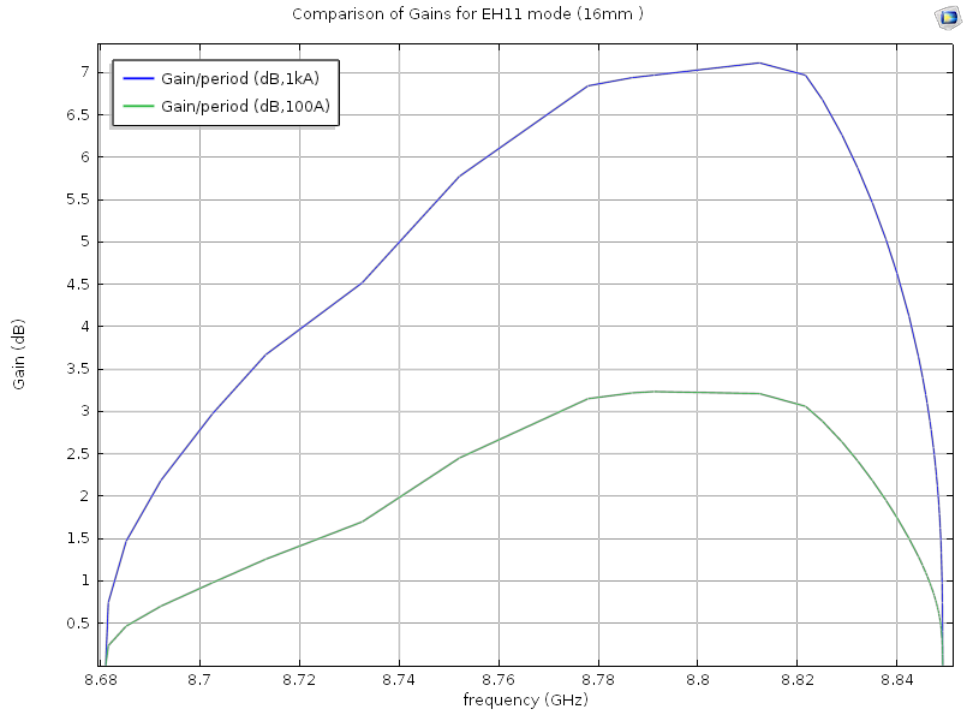

FIGURE 5.11. ratio 3.2, depth ribbed structure, gain per period curve

curve shown in Figure 5.7, we get the gain curve 5.11, which starts from zero and increases as one moves down the dispersion curve, attains a maximum at the slip Δk close to zero (see Table 5.3), then decreases to zero. In Figure 5.11, the x-axis is frequency in GHz and the y-axis is in decibels.

TABLE 5.3. Data at slip = 0.26995

	$I = 100$ A	$I = 1000$ A
ω_0 (rad/s)	$5.536969260769897 \times 10^{10}$	
f_0	8.812360275994066 GHz	
Im$\{\delta k\}$	0.3698	0.8192
Gain factor	3.212	7.1155
α	0.035872	0.35872
${K_0}^3$	-0.086801	-0.86801

misalign elliptical

When we compute the gain per period by picking on the dispersion curve shown

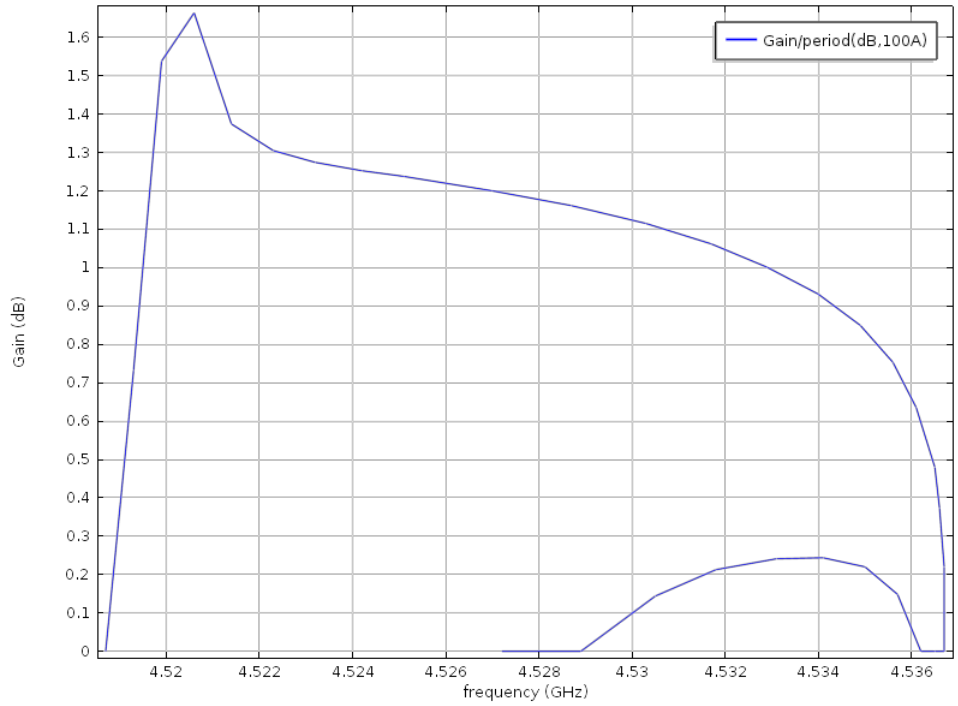

FIGURE 5.12. Current 100A: Gain per period at the DBE

in the figure 5.8 (b), we get the gain curve Figure 5.12. Which starts from zero and increases as one moves up along the forward wave, attains a maximum at the slip mentioned in Table 5.4 then decreases to zero at the point called DBE. Increases again as we move down the backward wave, attains a maximum at the DBE frequency then decreases to zero. In Figure 5.12 the x-axis is frequency in GHz and the y-axis is decibels.

TABLE 5.4. Data at slip = -0.059283

	$I = 100$ A	$I = 1000$ A
ω_0 (rad/s)	2.8404×10^{10}	
f_0	4.5206 GHz	
$\mathrm{Im}\{\delta k\}$	0.1915949838912495	0.41551709847985024
Gain factor	1.6642	3.6091
α	0.78618	1.7707
${K_0}^3$	-0.11103	-0.011103

5.6 conclusion

The discussed 3^{rd} order reduced model is working because of the two reasons. First, the cold structure simulation recovers the dispersion curves discussed in [12] and [23]. And second, the pattern of the gain factor curves discussed in Section 5.5 matches with those in [19]. When the depth of the rib is increased from ratio 2.4 to 3.2, the gain factor increases. the reason is the synchronization of the increasing strength of the z-component of the $\mathbf{V}^0$ field with the electron beam as the depth increases from ratio 2.4 to 3.2. On further increase of the depths the gain factor decreases. Our model also shows the maximum gain at the DBE frequency, which agrees with the result shown in [23]

References

[1] G. Kristensson, *Homogenization of corrugated interfaces in electromagnetics*, Progress In Electromagnetic Research, Pages:1–31, Vol.55, 2005.

[2] J. Nevard and J. B. Keller, *Homogenization of rough boundries and interfaces*, SIAM J. Appl. Math., Num.6, Pages: 1660–1686, Vol.57, 1997.

[3] W. E. Kohler and G. C. Papanicolaou and S. Varadhan, *Boundary and interface problems in regions with very rough boundaries*, Multiple Scattering and Waves in Random Media, Pages: 165–198, Publisher: North Holland, 1981.

[4] E. Sanchez-Palencia, *Non-Homogeneous Media and Vibration Theory*, Publisher: Springer-Verlag, Series: Lecture Notes in Physics, Vol.127, 1980.

[5] L. Schächter, *Beam-Wave Interaction in Periodic and Quasi-Periodic Structures*, Publisher: Springer-Verlag, Series: Particle Accelerators and Detection, 2011.

[6] A. Bensoussan and J. L. Lions and G. Papanicolaou, *Asymptotic Analysis for Periodic Structures*, Publisher: North Holland, Series: Studies in Mathematics and its Applications, Vol. 5, 1978.

[7] J. B. Pendry and J. A. Holden and J. D. Robbins and W. J. Stewart, *Magnetism from conductors and enhanced nonlinear phenomena*, Journal: IEEE Trans. Microw. Theory Tech., Pages: 2075–2084, Vol.47, 1999.

[8] Tamara G. Kolda and Jackson R. Mayo, *An Adaptive Shifted Power Method for Computing Generalized Tensor Eigenpairs*, Journal: SIAM Journal on Matrix Analysis and Applications, Pages: 1563–1581, Vol.35, 2014,

[9] P. J. B. Clarricoats and P. K. Saha, *Propagation and radiation behaviour of corrugated feeds. Part 1: Corrugated-waveguide feed*, Journal: Proceedings of the Institution of Electrical Engineers, Pages: 1167–1176, Vol.118, 1971,

[10] P. J. B. Clarricoats and M. I. Sobhy, *Propagation behaviour of periodically loaded waveguides*, Journal: Proceedings of the Institution of Electrical Engineers, Num.5, Pages: 652–651, Vol.115, 1968.

[11] E. García and J.A. Murphy and E. de Lera and D. Segovia, *Analysis of the left-handed corrugated circular waveguide*, Journal: IET Microwaves, Antennas & Propagation, Month = apr, Num.7, Pages: 659–667, Vol.2, 2008,

[12] S. C. Yurt and A. Elfrgani and M. I. Fuks and K. Ilyenko and E. Schamiloglu, *Similarity of Properties of Metamaterial Slow-Wave Structures and Metallic Periodic Structures*, Journal: IEEE Transactions on Plasma Science, Num.99, Pages: 1-7, 2016.

[13] G. Stupakov and K. L. F. Bane, *Surface impedance formalism for a metallic beam pipe with small corrugations*, Journal: Physical Review Special Topics - Accelerators and Beams, Month = sep, Pages: 124401-1–124401-9, Vol.15, 2012.

[14] J. L. Doane, *Propagation and Mode Coupling in Corrugated and Smooth-Wall Circular Waveguides*, *Booktitle: Infrared and Millimeter Waves, Volume 13, Millimeter Components and Techniques Part IV*, Chapter = 5, Editor: K. J. Button, Pages: 123-170, Publisher: Academic Press, 1985.

[15] David M. Pozar, *Microwave Engineering*, Edition: second, Publisher: John Wiley & Sons, 1998.

[16] D. Shiffler and J. Luginsland and D.M. French and J. Waltrous, *A Cerenkov-like Maser Based on a Metamaterial Structure*, Journal: IEEE Trans. Plasma Sci., Pages: 1462–1465, Vol.38, 2010.

[17] James E. Brittain, *Electrical Engineering Hall Of Fame, JOHN R. PIERCE*, Journal: Proceedings of the IEEE, Vol.98, 2010.

[18] L.J.Chu and D.Jackson, *Field theory of traveling-wave tube*, Technical report no.39, April 28, 1947.

[19] Levi Schächter, John.A.Nation, and Graham Kerslick, *On the bandwidth of a short traveling wave tube*, J.Appl.Phys. Vol.68,No.11, 1st December 1990.

[20] Robert Lipton and Anthony Polizzi, *Tuning gain and bandwidth of traveling wave tubes using metamaterial beam-wave interaction structures*, J. Appl. Phys. 116, 144504 (2014); doi: 10.1063/1.4897235

[21] Joseph A. Eichmeier and Manfred Thumm, *Vacuum Electronic Components and Devices*, Springer, ISBN 978-3-540-71928-1

[22] Edl Schamiloglu, *Dispersion Engineering for High Power Microwave Amplifiers*, Dept. of Electrical and Computer Engineering, University of New Mexico.

[23] Mohamed A. K Othman, Xuyuan Pan, Georgics Atmatzakis, Christos Christodoulou and Filippo Capolino, *Experimental Demonstration of Degenerate Ban Edge in Metallic Periodically-Loaded Circular Waveguide*, UC IRVINE, Nov. 2016.

Appendix: Derivation of Homogenized Problem

In this section we derive the leading order transmission boundary value problem 4.8 - 4.16 using two-scale expansions.

A. 1 Maxwell's equations in local coordinates

Again using the definition of the fast variable $y = z/d$ so that $\partial_z \to \partial_z + d^{-1}\partial_y$,

$$\begin{cases} \nabla\times\mathbf{E} & = \vec{e}_r(\frac{1}{r}\partial_\varphi E_z - (\partial_z + d^{-1}\partial_y)E_\varphi) \\ & \quad +\vec{e}_\varphi((\partial_z + d^{-1}\partial_y)E_r - \partial_r E_z) + \vec{e}_z(\frac{1}{r}\partial_r(rE_\varphi) - \frac{1}{r}\partial_\varphi E_r) \\ & = -i\omega(B_r\vec{e}_r + B_\varphi\vec{e}_\varphi + B_z\vec{e}_z), \\ \nabla\times\mathbf{B} & = \vec{e}_r(\frac{1}{r}\partial_\varphi B_z - (\partial_z + d^{-1}\partial_y)B_\varphi) \\ & \quad +\vec{e}_\varphi((\partial_z + d^{-1}\partial_y)B_r - \partial_r B_z) + (\frac{1}{r}\partial_r(rB_\varphi) - \frac{1}{r}\partial_\varphi B_r) \\ & = i\omega\mu_0\epsilon_0(E_r\vec{e}_r + E_\varphi\vec{e}_\varphi + E_z\vec{e}_z), \\ \nabla\cdot\mathbf{E} & = \frac{1}{r}\partial_r(rE_r) + \frac{1}{r}\partial_\varphi E_\varphi + (\partial_z + d^{-1}\partial_y)E_z = 0, \\ \nabla\cdot\mathbf{B} & = \frac{1}{r}\partial_r(rB_r) + \frac{1}{r}\partial_\varphi B_\varphi + (\partial_z + d^{-1}\partial_y)B_z = 0. \end{cases} \tag{5.17}$$

For $r_m < r < r_m + h$ the fast variable y lies in the waveguide between the corrugations. This is written as the union of intervals $-1/2 < y < y_-(r)$ and $y_+(r) < y < 1/2$ and this union is denoted by $Y(r)$. The width between corrugations $\theta(r)$ is given by $\theta(r) = 1 - (y_+(r) - y_r(r))$. The interval $[-1/2, 1/2]$ is denoted by Y and y values outside the waveguide are given by the interval $y_-(r) < y < y_+(r)$ or $Y \setminus Y(r)$ for $r_m < r < r_m + h$. The perfectly conducting boundary is $y = y_\pm(r)$. Part of the corrugations on $r = r_m$ can be flat sections of perfect conductor and this corresponds to $y_-(r_m) < y < y_+(r_m)$ or $Y \setminus Y(r_m)$. Similarly at $r = r_m + h$ there are flat parts and this corresponds with $Y(r_m + h)$ given by the union $-1/2 < y < y_-(r_m + h)$ and $y_+(r_m + h) < y < 1/2$.

It is also convenient to write boundary of the corrugation as a function of y. The boundary is written $r = r_m + h(y)$ and recalling $y = x/d$ we get the formula for the normal vector to $y_\pm(r)$ given by

$$\vec{\nu} = \frac{-d^{-1}\partial_y h(y)\vec{e}_z + \vec{e}_r}{(1 + d^{-2}(\partial_y h(y))^2)^{1/2}}. \tag{5.18}$$

For future reference, it is easily seen that

$$\begin{cases} y'(r) & = \frac{1}{\partial_y h(y)}, \\ \theta'(r) & = y'_-(r) - y'_+(r). \end{cases} \tag{5.19}$$

With these preliminaries in hand, we describe boundary conditions on the waveguide boundary. On $y = y_\pm(r)$, $r_m < r < r_m + h$, the perfect conducting boundary conditions become

$$\begin{cases} \vec{\nu}\cdot\mathbf{B}^I & = \frac{-d^{-1}\partial_y h(y)B^I_z + B^I_r}{(1+d^{-2}(\partial_y h(y))^2)^{1/2}} = 0, \\ \vec{\nu}\times\mathbf{E}^I & = \frac{d^{-1}(\vec{e}_r\partial_y h E^I_\varphi - \vec{e}_\varphi\partial_y h E^I_r)}{(1+d^{-2}(\partial_y h(y))^2)^{1/2}} + \vec{e}_z E^I_\varphi - \vec{e}_\varphi E^I_z = 0, \end{cases} \tag{5.20}$$

for $r = r_m$ and y on $Y \setminus Y(r_m)$

$$\begin{cases} \vec{e}_r \times \mathbf{E}^W &= \vec{e}_z E_\varphi^W - \vec{e}_\varphi E_z^W = 0, \\ \vec{e}_r \cdot \mathbf{B}^W &= B_r^W = 0, \end{cases} \tag{5.21}$$

and for $r = r_m + h$ and y on $Y(r_m + h)$

$$\begin{cases} \vec{e}_r \times \mathbf{E}^I &= \vec{e}_z E_\varphi^I - \vec{e}_\varphi E_z^I = 0, \\ \vec{e}_r \cdot \mathbf{B}^I &= B_r^I = 0. \end{cases} \tag{5.22}$$

We denote the operators ∇ and $\nabla\times$ expressed in terms of slow cylindrical variables r, φ, z by $\nabla_{\mathbf{x}}$ and $\nabla_{\mathbf{x}}\times$. Applying (5.17), we have for $\mathbf{E}$ and $\mathbf{B}$ denoting $\mathbf{E}^W, \mathbf{B}^W$ and $\mathbf{E}^I, \mathbf{B}^I$ we get the system

$$\begin{cases} \nabla\times\mathbf{E} &= \nabla_{\mathbf{x}} \times \mathbf{E} + d^{-1}(-\vec{e}_r \partial_y E_\varphi + \vec{e}_\varphi \partial_y E_r) = -i\omega\mathbf{B}, \\ \nabla\times\mathbf{B} &= \nabla_{\mathbf{x}} \times \mathbf{B} + d^{-1}(-\vec{e}_r \partial_y B_\varphi + \vec{e}_\varphi \partial_y B_r) = i\omega\mu_0\epsilon_0\mathbf{E}, \\ \nabla \cdot \mathbf{E} &= \nabla_{\mathbf{x}} \cdot \mathbf{E} + d^{-1}\partial_y E_z = 0, \\ \nabla \cdot \mathbf{B} &= \nabla_{\mathbf{x}} \cdot \mathbf{B} + d^{-1}\partial_y B_z = 0. \end{cases} \tag{5.23}$$

In the next section we substitute in the two-scale expansion into 5.8, 4.6, and 5.20 - 5.23 and equate like powers of d to obtain a system of equations for determining the leading order theory.

A. 2 Asymptotic theory

Substitution of expansions (4.7) into equations (5.20), (5.22) and (5.23) gives (for $\mathbf{E} = \mathbf{E}^W$ or $\mathbf{E} = \mathbf{E}^I$ and $\mathbf{B} = \mathbf{B}^W$ or $\mathbf{B} = \mathbf{B}^I$)

$$\nabla_{\mathbf{x}} \times \mathbf{E}^{j-1} - \vec{e}_r \partial_y E_\varphi^j + \vec{e}_\varphi \partial_y E_r^j = -i\omega\mathbf{B}^{j-1}, \tag{5.24a}$$

$$\nabla_{\mathbf{x}} \times \mathbf{B}^{j-1} - \vec{e}_r \partial_y B_\varphi^j + \vec{e}_\varphi \partial_y B_r^j = i\omega\mu_0\epsilon_0\mathbf{E}^{j-1}, \tag{5.24b}$$

$$\nabla_{\mathbf{x}} \cdot \mathbf{E}^{j-1} + \partial_y E_z^j = 0, \tag{5.24c}$$

$$\nabla_{\mathbf{x}} \cdot \mathbf{B}^{j-1} + \partial_y B_z^j = 0, \tag{5.24d}$$

and on $y = y_\pm(r)$,

$$\begin{cases} -\vec{e}_\varphi E_z^{I(j-1)} + \vec{e}_z E_\varphi^{I(j-1)} + \partial_y h(-\vec{e}_\varphi E_r^{Ij} + \vec{e}_r E_\varphi^{Ij}) = 0, \\ -\partial_y h B_z^{Ij} + B_r^{I(j-1)} = 0, \end{cases} \tag{5.25}$$

and, at $r = r_m + h$ and y on $Y(r_m + h)$:

$$E_\varphi^{Ij} = 0, \qquad E_z^{Ij} = 0, \qquad B_r^{Ij} = 0. \tag{5.26}$$

At $r = r_m$ and for $j = 0$ applying 4.6 gives

$$\begin{cases} -\langle E_\varphi^{W0} - E_\varphi^{I0}\rangle \vec{e}_z + \langle E_z^{W0} - E_z^{I0}\rangle \vec{e}_\varphi = 0, \\ -\langle B_\varphi^{W0} - B_\varphi^{I0}\rangle \vec{e}_z + \langle B_z^{W0} - B_z^{I0}\rangle \vec{e}_\varphi = J_z \vec{e}_z + J_\varphi \vec{e}_\varphi, \\ \langle \epsilon_0 E_r^{W0} - \epsilon_0 E_r^{I0}\rangle = \rho, \\ \langle B_r^{W0} - B_r^{I0}\rangle = 0. \end{cases} \tag{5.27}$$

and for $j > 0$

$$\begin{cases} -\langle E_\varphi^{Wj} - E_\varphi^{Ij}\rangle \vec{e}_z + \langle E_z^{Wj} - E_z^{Ij}\rangle \vec{e}_\varphi = 0, \\ -\langle B_\varphi^{Wj} - B_\varphi^{Ij}\rangle \vec{e}_z + \langle B_z^{Wj} - B_z^{Ij}\rangle \vec{e}_\varphi = 0, \\ \langle \epsilon_0 E_r^{Wj} - \epsilon_0 E_r^{Ij}\rangle = 0, \\ \langle B_r^{Wj} - B_r^{Ij}\rangle = 0. \end{cases} \tag{5.28}$$

and from 5.8 and 5.21 for $r = r_m$ and y in $Y \setminus Y(r_m)$ and $j \geq 0$,

$$\begin{cases} \vec{e}_z E_\varphi^{Ij} - \vec{e}_\varphi E_z^{Ij} = 0, \\ B_r^{Ij} = 0, \end{cases} \tag{5.29}$$

and

$$\begin{cases} \vec{e}_z E_\varphi^{Wj} - \vec{e}_\varphi E_z^{Wj} = 0, \\ B_r^{Wj} = 0. \end{cases} \tag{5.30}$$

Here we use the convention that $\mathbf{E}^j, \mathbf{B}^j \equiv 0$ for $j < 0$.

A. 3 $j = 0$ **Theory**

The zero-order theory, *i.e.*, equation (5.24a) with $j = 0$ gives

$$-\vec{e}_r \partial_y E_\varphi^0 + \vec{e}_\varphi \partial_y E_r^0 = 0, \tag{5.31}$$

which holds for $\mathbf{E} = \mathbf{E}^{W0}$ and $\mathbf{E} = \mathbf{E}^{I0}$, while equation (5.24b) for $\mathbf{B}^{W0}$, $\mathbf{B}^{I0}$ yields

$$-\vec{e}_r \partial_y B_\varphi^0 + \vec{e}_\varphi \partial_y B_r^0 = 0. \tag{5.32}$$

Equations (5.24c) and (5.24d) for both $\mathbf{B} = \mathbf{B}^{W0}, \mathbf{B}^{I0}$ and $\mathbf{E} = \mathbf{E}^{W0}, \mathbf{E}^{I0}$ yield

$$\partial_y E_z^0 = 0, \qquad \partial_y B_z^0 = 0. \tag{5.33}$$

On the boundary, $y_\pm(r)$, $r_m < r < r_m + h$ we have

$$-\vec{e}_\varphi E_r^{I0} + \vec{e}_r E_\varphi^{I0} = 0, \qquad -B_z^{I0} = 0, \tag{5.34}$$

so for y in Y and $0 < r < r_m$ and for y in $Y(r_m)$ and $r = r_m$,

$$\begin{array}{lll} E_r^{W0} = E_r^{W0}(z,r,\varphi), & E_z^{W0} = E_z^{W0}(z,r,\varphi), & E_\varphi^{W0} = E_\varphi^{W0}(z,r,\varphi), \\ B_r^{W0} = B_r^{W0}(z,r,\varphi), & B_z^{W0} = B_z^{W0}(r,z,\varphi), & B_\varphi^{W0} = B_\varphi^{W0}(r,z,\varphi). \end{array} \tag{5.35}$$

and for y in $Y(r)$ and $r_m < r \leq r_m + h$

$$\begin{array}{lll} E_r^{I0} = E_r^{I0}(z,r,\varphi), & E_z^{I0} = E_z^{I0}(z,r,\varphi), & E_\varphi^{I0} = E_\varphi^{I0}(z,r,\varphi), \\ B_r^{I0} = B_r^{I0}(z,r,\varphi), & B_z^{I0} = B_z^{I0}(r,z,\varphi), & B_\varphi^{I0} = B_\varphi^{I0}(r,z,\varphi). \end{array} \tag{5.36}$$

Applying the boundary condition (5.34) shows that for $r_m < r \leq r_m + h$ and y in $Y(r)$ that

$$E_r^{I0}(z,r,\varphi) = 0, \qquad E_\varphi^{I0}(z,r,\varphi) = 0, \qquad B_z^{I0}(z,r,\varphi) = 0. \tag{5.37}$$

So, in the impedance layer $r_m < r < r_m + h$, y in $Y(r)$, we have

$$\begin{cases} \mathbf{E}^{I0} & = \vec{e}_z E_z^{I0}(z, r, \varphi), \\ \mathbf{B}^{I0} & = \vec{e}_\varphi B_\varphi^{I0}(z, r, \varphi) + \vec{e}_r B_r^{I0}(z, r, \varphi), \end{cases} \tag{5.38}$$

with (from the boundary condition at $r = r_m + h$)

$$\begin{cases} E_z^{I0}(z, r_m + h, \varphi) = 0, \\ B_r^{I0}(z, r_m + h, \varphi) = 0. \end{cases} \tag{5.39}$$

This establishes 4.9 and 4.11. The interface conditions at $r = r_m$ given by 4.10 now follow from a straightforward calculation using 5.8, 5.27, 5.29, 5.30, 5.35, 5.36, and 5.37. In the following section we recover the differential equations satisfied by the leading order theory.

A. 4 $j = 1$ Theory

In this final section we recover the differential equations 4.8, 4.12, 4.15, and 4.16 satisfied by $\mathbf{E}^{W0}$, $\mathbf{B}^{W0}$, $\mathbf{E}^{I0}$, and $\mathbf{B}^{I0}$. Start with equation (5.24a) in both the interior waveguide and in the impedance layer and we have

$$\nabla_{\mathbf{x}} \times \mathbf{E}^0 + (-\vec{e}_r \partial_y E_\varphi^1 + \vec{e}_\varphi \partial_y E_r^1) = -i\omega \mathbf{B}^0. \tag{5.40}$$

For $0 < r < r_m$ we integrate 5.40 in the y variable over Y and note that $\mathbf{E}^{W1}$ is periodic in y while $\mathbf{E}^{W0}$, $\mathbf{B}^{W0}$ are independent of y to recover the equation,

$$\nabla_{\mathbf{x}} \times \mathbf{E}^{W0} = -i\omega \mathbf{B}^{W0}, \qquad 0 < r < r_m. \tag{5.41}$$

For $r_m < r < r_m + h$, in the impedance layer, we integrate 5.40 over $-1/2 < y < y^-(r)$ and over $y^+(r) < y < 1/2$:

$$\int_{-1/2}^{y^-(r)} \nabla_{\mathbf{x}} \times \mathbf{E}^{W0} \, \mathrm{d}y + \left(-\vec{e}_r \int_{-1/2}^{y^-(r)} \partial_y E_\varphi^{W1} \, \mathrm{d}y + \vec{e}_\varphi \int_{-1/2}^{y^-(r)} \partial_y E_r^{W1} \, \mathrm{d}y \right) = -i\omega \int_{-1/2}^{y^-(r)} \mathbf{B}^{W0} \, \mathrm{d}y \tag{5.42}$$

$$\int_{y^+(r)}^{1/2} \nabla_{\mathbf{x}} \times \mathbf{E}^{W0} \, \mathrm{d}y + \left(-\vec{e}_r \int_{y^+(r)}^{1/2} \partial_y E_\varphi^{W1} \, \mathrm{d}y + \vec{e}_\varphi \int_{y^+(r)}^{1/2} \partial_y E_r^{W1} \, \mathrm{d}y \right) = -i\omega \int_{y^+(r)}^{1/2} \mathbf{B}^{W0} \, \mathrm{d}y \tag{5.43}$$

We add equations (5.42) and (5.43) noting that $\mathbf{E}^{W0}$ and $\mathbf{B}^{W0}$ are independent of y and apply

$$\theta(r) = \int_{-1/2}^{y^-(r)} \mathrm{d}y + \int_{y^+(r)}^{1/2} \mathrm{d}y, \tag{5.44}$$

to get

$$\theta(r)\nabla_{\mathbf{x}}\times\mathbf{E}^0+\int_{y^+(r)}^{1/2}(-\vec{e}_r\partial_y E^1_\varphi+\vec{e}_\varphi\partial_y E^1_r)\,\mathrm{d}y \\ +\int_{-1/2}^{y^-(r)}(-\vec{e}_r\partial_y E^1_\varphi+\vec{e}_\varphi\partial_y E^1_r)\,\mathrm{d}y=-i\omega\theta(r)\mathbf{B}^0.$$

Since $\mathbf{E}^{I1}$ is Y periodic we get

$$\nabla_{\mathbf{x}}\times\mathbf{E}^{I0}+\theta^{-1}(r)(-\vec{e}_r(E^1_\varphi(y^-(r))-E^1_\varphi(y^+(r))) \\ +\vec{e}_\varphi(E^1_r(y^-(r))-E^1_r(y^+(r))))=-i\omega\mathbf{B}^{I0}. \quad (5.45)$$

From the boundary condition (5.25), for $r_m<r<r_m+h$, we deduce the scalar equations

$$E^{I0}_r(y_\pm,z,r,\varphi)=-\frac{1}{\partial_y h(y_\pm)}E^{I0}_z(z,r,\varphi), \quad (5.46)$$

$$E^{I1}_\varphi(y_\pm,z,r,\varphi)=0, \quad (5.47)$$

and from earlier work, we have

$$E^{I0}_\varphi(z,r,\varphi)=0,\qquad r_m<r<r_m+h.$$

Now, applying 5.19 and collecting results gives

$$\vec{e}_\varphi(-\partial_r E^{I0}_z-\theta^{-1}(r)\partial_r\theta(r)E^{I0}_z)+\vec{e}_r(\frac{1}{r}\partial_\varphi E^{I0}_z)=-i\omega(\vec{e}_r B^{I0}_r+\vec{e}_\varphi B^{I0}_\varphi), \quad (5.48)$$

for $r_m<r<r_m+h$. Taking the dot product of equation (5.48) with unit vector $\vec{e}_r$ in the impedance layer yields

$$\frac{1}{r}\partial_\varphi E^{I0}_z=-i\omega B^{I0}_r,\quad r_m<r<r_m+h, \quad (5.49)$$

and the dot product of (5.48) with unit vector $\vec{e}_\varphi$ and elemetary manipulation yields

$$\partial_r(\theta(r)E^{I0}_z)=\theta(r)i\omega B^{I0}_\varphi,\quad r_m<r<r_m+h. \quad (5.50)$$

Apply 5.24b with $j=1$ for $0<r<r_m$ to write

$$\nabla_{\mathbf{x}}\times\mathbf{B}^{W0}-\vec{e}_r\partial_y B^{W1}_\varphi+\vec{e}_\varphi\partial_y B^{W1}_r=i\omega\mu_0\epsilon_0\mathbf{E}^{W0}.$$

As before integrate both sides of this equation with respect to y over Y, noting that B^{W1}_φ and B^{W1}_r are periodic with respect to y and $\mathbf{B}^{W0}$ and $\mathbf{E}^{W0}$ are y independent to see that

$$\nabla_{\mathbf{x}}\times\mathbf{B}^{W0}=i\omega\mu_0\epsilon_0\mathbf{E}^{W0},\qquad 0<r<r_m. \quad (5.51)$$

Inside the impedance layer $r_m < r < r_m + h$, the $j = 1$ theory for 5.24b gives

$$\nabla_{\mathbf{x}} \times \mathbf{B}^{I0} - \vec{e}_r \partial_y B_\varphi^{I1} + \vec{e}_\varphi \partial_y B_r^{I1} = i\omega\mu_0\epsilon_0 \mathbf{E}^{I0}.$$

Taking the dot product with $\vec{e}_z$ yields

$$\frac{1}{r}\partial_r(rB_\varphi^{I0}) - \frac{1}{r}\partial_\varphi B_r^{I0} = i\omega\mu_0\epsilon_0 E_z^{I0}. \tag{5.52}$$

In the inner waveguide, $0 < r < r_m$ the $j = 1$ theory for 5.24c gives

$$\nabla_{\mathbf{x}} \cdot \mathbf{E}^{W0} + \partial_y E_z^{W1} = 0.$$

Again, integrating this equation over $y \in Y$ and using the y-periodicity of E_z^{W1} gives us

$$\nabla_{\mathbf{x}} \cdot \mathbf{E}^{W0} = 0, \qquad 0 < r < r_m. \tag{5.53}$$

Similarly we can apply 5.24d to find

$$\nabla_{\mathbf{x}} \cdot \mathbf{B}^{W0} = 0, \qquad 0 < r < r_m. \tag{5.54}$$

Now applying the $j = 1$ theory for 5.24d inside the impedance layer, $r_m < r < r_m + h$ we have

$$\nabla_{\mathbf{x}} \cdot \mathbf{B}^{I0} + \partial_y B_z^{I1} = 0.$$

Here, $\mathbf{B}^{I0} = \vec{e}_r B_r^{I0}(z, r, \varphi) + \vec{e}_\varphi B_\varphi^{I0}(z, r, \varphi)$, and, in local coordinates, we get

$$\frac{1}{r}\partial_r(rB_r^{I0}) + \frac{1}{r}\partial_\varphi B_\varphi^{I0} + \partial_y B_z^{I1} = 0.$$

At the boundaries $y_\pm(r)$, for the $j = 1$ theory for 5.25 gives

$$\partial_y h(y_\pm) B_z^{I1}(y_\pm(r), z, r, \varphi) = B_r^{I0}(z, r, \varphi), \tag{5.55}$$

and integrating (5.55) over $-1/2 < y < y_-(r)$ and $y_+(r) < y < 1/2$ (and adding the results) gives

$$\begin{aligned}\theta(r)(\frac{1}{r}\partial_r(rB_r^{I0}) + \frac{1}{r}\partial_\varphi B_\varphi^{I0}) + B_z(y^-(r), z, r, \varphi) - B_z^{I1}(-1/2, z, r, \varphi) \\ + B_z^{I1}(1/2, z, r, \varphi) - B_z^{I1}(y^+(r), z, r, \varphi) = 0.\end{aligned} \tag{5.56}$$

Applying (5.19) and (5.55) gives the string of equalities

$$\begin{aligned}B_z^{I1}(y_-(r), z, r, \varphi) - B_z^{I1}(y_+(r), z, r, \varphi) &= \left(\frac{1}{\partial_y h(y_-)} - \frac{1}{\partial_y h(y_+)}\right) B_r^{I0}(z, r, \varphi) \\ &= (\partial_r y_-(r) - \partial_r y_+(r)) B_r^{I0}(z, r, \varphi) \\ &= \partial_r \theta(r) B_r^{I0}(z, r, \varphi),\end{aligned}$$

and we arrive at the equation

$$\theta(r)(\frac{1}{r}\partial_r(rB_r^{I0}) + \frac{1}{r}\partial_\varphi B_\varphi^{I0}) + \partial_r\theta(r) B_r^{I0}(z, r, \varphi) = 0. \tag{5.57}$$

In summary we have recovered 4.8 from 5.41, 5.51, 5.53, and 5.54. Equations 4.15, 4.16 follow from 5.49 and 5.50. We then substitute 4.15 and 4.16, into 5.57 to see that 5.57 is satisfied identically. Last we recover 4.12 on substituting 4.15, 4.16 into 5.52.

Vita

Lokendra Singh Thakur was born in Hyderabad City, INDIA. He completed his undergraduate degree with major in chemistry and minor in biology and finished master of business administration specializing in finance. He earned a master of science degree in mathematics from Louisiana State University in May 2012. In August 2012 he returned to Louisiana State University to pursue graduate studies in mathematics. He is currently a candidate for the degree of Doctor of Philosophy in mathematics, which will be awarded in August 2017.